Dipolar interactions, long range order and random fields in a single molecule magnet, Mn12-acetate

by

Bo Wen

A dissertation submitted to the Graduate Faculty in Physics in partial fulfillment of the requirements for the degree of Doctor of Philosophy, The City University of New York.

2013

This manuscript has been read and accepted for the Graduate Faculty in Physics in satisfaction of the dissertation requirement for the degree of Doctor of Philosophy.

Date	Prof. Myriam P. Sarachik Chair of Examining Committee
Date	Prof. Steven Greenbaum Executive Officer

Prof. Eugene M. Chudnovsky

Prof. Morrel H. Cohen

Prof. Andrew D. Kent

Prof. Sergey Vitkalov

Supervisory Committee

THE CITY UNIVERSITY OF NEW YORK

Abstract

Dipolar interactions, long range order and random fields in a single molecule magnet, Mn_{12}-acetate

by

Bo Wen

Thesis Advisor: Distinguished Professor Myriam P. Sarachik

In this thesis, I will present an experimental study of two single molecule magnets, Mn_{12}-ac and Mn_{12}-ac-MeOH. I will show that in both systems, the temperature dependence of the inverse susceptibility yields a positive intercept on the temperature axis (a positive Weiss temperature), implying the existence of a ferromagnetic phase at low temperature.

Applying a magnetic field in the transverse direction moves the Weiss temperature downward towards zero. This implies that the transverse field triggers mechanisms in the system that compete with the dipolar interaction and suppress the long-range ordering.

I will then show that the suppression in Mn_{12}-ac is considerably stronger than that expected for a pure TFIFM (Transverse Field Ising Ferromagnetic) model system. By contrast, the behavior of Mn_{12}-ac-MeOH is consistent with the model.

We attribute the difference between the two systems to the presence of randomness in Mn_{12}-ac associated with isomer disorder. Thus, in addition to spin-canting and thermal fluctuations, which contribute to the suppression of long-range order in both materials in the same way, the random fields due to isomer disorder that exist in Mn_{12}-ac and not in Mn_{12}-ac-MeOH causes further suppression of ferromagnetism in Mn_{12}-ac. The behavior observed for Mn_{12}-ac is consistent with a random field model calculated for this system by Millis et al.

To my wife, Rose,

for her fathomless love,

and "Boson" Solon,

for all the happiness he brings to us.

Acknowledgments

"*Philosophia* etymologically connotes the love of exercising one's curiosity and intelligence rather than the love of wisdom." –*The Encyclopedia of Philosophy*

I believe that every Ph.D. owns a unique memory from his/her few-years Ph.D. life. While the road to earning a Ph.D. requires sacrifice, sleepless nights, and a very strong work ethic, these are not the things most memorable to me. Instead, my fondest memories are of all the remarkable people I met on this journey, so I would like to give gratitude to all of these individuals who have had such a strong impact on my life and work.

First, I would like to thank my mentor, distinguished professor of physics, Myriam P. Sarachik. She guided me through many of my trials and tribulations, both academically and personally. She provided me with many opportunities and supported me with all the resources she had. I could not have hoped for a better mentor or friend.

The trajectory of my life would probably have been much different if it were not for my middle school physics teacher Mr. Jinghong Ho. He always told us that "science starts with taking a bold guess, then test it out carefully". I am always good at the first part, but still working on the second part.

Prof. Alexander Shashkin from ISSP RAS played a major role in helping me lay the groundwork as a scientist. He showed me how to systematically identify problems and use step-by-step methods to solve them. He stressed the importance of recording everything in a lab book, checking off each step, one at a time. Patience was the theme for the three months we worked together.

Prof. Andy Kent of NYU and Prof. Yosi Yeshurun of Bar-Ilan University are the

major collaborators of the experimental work of this thesis. They both jumped off the cliff with me on this project, and without them providing the parachute and guidance, the landing would have likely been messy.

Prof. George Christou and his students from University of Florida provided all the SMM samples for us to study and play with. I am also very much appreciative of the invitation to and his hospitality for the 2010 CTMNM conference.

As a student, I am deeply indebted to my advisers: Prof. Alexander Punnoose (CCNY, now IFT-UNESP), Prof. Sergey Vitkalov(CUNY CCNY), Prof. Andy Millis (Columbia University), Prof. Demitry Garanin (CUNY Lehman), Prof. Eugene Chudnovsky (CUNY Lehman), and Prof. Morrel Cohen (Princeton and Rutgers). Each one of these individuals guided me at various points along the way. I will always remember what Morrel told me: "When you can't find an answer, check if you are asking the right question."

In addition to my advisers, I gained a lot of helps and supports from my fellow student collegues and friends: Sean McHugh, Pradeep Subedi, Alexander Kapustin, Arjun Narayanan, Jean-Marc Beaujour, Lukas Zhao, Shiqi Li, Lin Bo, Wei Liu, Gabriel Chaves, Gregoire De LOUBENS and et al. I learned to never underestimate the amount of creativity and productivity of discussions over food and drinks.

Additionally, I would also like to thank the following individuals, each who provided me with invaluable advice and inspiration. I can safely say that I would not have gotten so far to where I am today without them: Prof. Timothy Boyer (CUNY CCNY), Prof. Brian Schwartz (CUNY), Prof. Lia Krusin-Elbaum (CUNY CCNY), Prof. William Halperin (Northwestern University), Prof. Sergey Kravchenko (Northeastern University), Dr. Enric Pardo (Slovak Academy of Sciences).

Last, but not least, none of this work would have been possible without generous financial support. I am grateful to NSF for their fundings to this project with grant numbers: NSF-DMR-0451605.

Contents

List of Tables

List of Figures

Chapter 1

Introduction

It has long been recognized that in addition to ferromagnetism due to quantum exchange interaction, dipolar interaction can also lead to long range ferromagnetic order. While dipolar interaction have been explored extensively for decades, both theoretically [1] and experimentally [2], recent interest has focused on quantum systems, where quantum fluctuations of the spins compete with the dipolar long range order.

1.1 Dipolar ferromagnetism in Single Molecule Magnets

Single Molecule Magnets (SMMs) are a class of metalorganic compounds, in which several transition metal ions are spatially structured by organic ligand molecules to form a central magnetic cluster. At low temperature, the spins of individual ions are coupled through super-exchange interaction to form a rigid giant spin.

This giant spin is much larger than the electron's spin ($S = \frac{1}{2}$), which behaves purely quantum mechanically. Yet, the giant spin is not large enough to display pure classical behavior. This feature makes SMM an excellent model system for studying the connections between the quantum world and classical worlds [3].

In a typical SMM, the magnetic cluster is surrounded by non-magnetic solvent molecules. As a result, the distance is large between neighboring magnetic clusters, which leads to the commonly held assumption in the early works of SMMs that the individual giant spins act independently. Such studies include the famous observation

of quantum tunneling of magnetization in Mn_{12}-acetate by Friedman, *et al.* in 1996 [4–6] and later in other SMMs [7–11], and the study of Berry phase oscillations in Fe_8 by Wernsdorfer, *et al.* in 1999 [12, 13] and other prototypical SMM. However, it is important to test the validity of the assumption that the molecules do not interact with each other.

Finite temperature transitions to a dipolar ferromagnetic state have been demonstrated in several SMMs [14–19]. In Mn_{12}-acetate (henceforth abbreviated as Mn_{12}-ac), the first-synthesized and best-studied example of a SMM, a transition to dipolar ferromagnetism was inferred from neutron scattering experiments by Luis *et al.* [15], and supported by Monte Carlo simulations [18] as well as calculations based on the Mean Field Approximation (MFA) [19].

1.2 Magnetic response of a SMM in a transverse field

In 2010, an in-depth study by our group of the suppression of the ferromagnetic order in a single crystal of Mn_{12}-ac by a magnetic field applied transverse to the crystal easy z-axis [20], gave a surprising result. As described in detail in Ch. 4 and shown here in Fig. 1.1, we attributed the observation to the presence of randomness and proposed a theory based on Random Field Ising Ferromagnet (RFIFM) model [21].

1.3 Random field in Mn_{12}-ac

The effect of random fields has been studied theoretically for many years. The essential feature of the random field is that it couples linearly to the order parameter, locally favoring one orientation over the other. Much theoretical work has been done in antiferromagnets following the observation of Fishman and Aharony [22] that in a site-diluted antiferromagnet, a spatially uniform applied transverse magnetic field produces a random field which acts on the antiferromagnetic order parameter. Despite

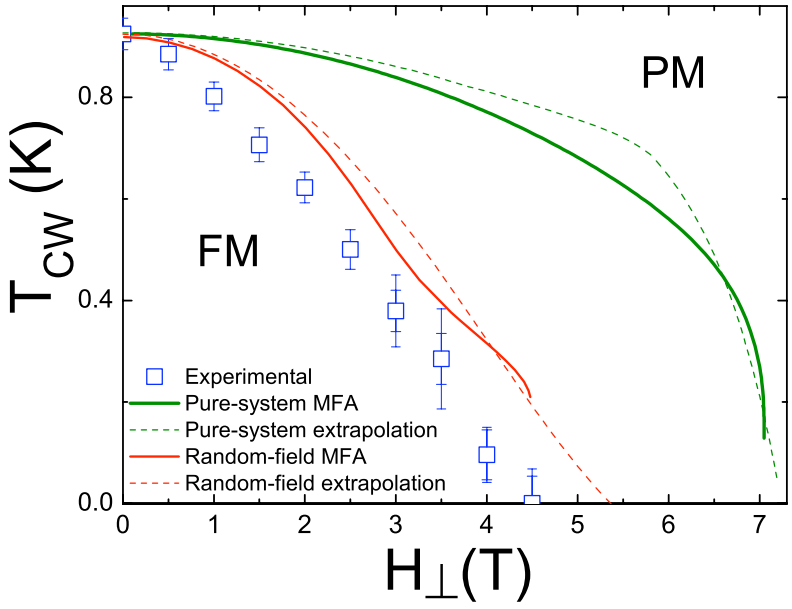

Figure 1.1: The Curie-Weiss and the ferromagnetic transition temperatures as a function of transverse field. The green line, which is the transition temperature predicted by a traditional MFA calculation based on a Transverse Field Ising Ferromagnet model (TFIFM), shows a weaker dependence on transverse field, while the blue dots, which is the experiment result, shows a much steeper suppression by the transverse field. However, the Random Field Ising Ferromagnet (RFIFM) model yields a fit much closer to the experimental observations, indicated by the red line.

the interest in this effect, there have been few experimental studies because of the difficulty of producing a magnetic field that varies randomly from site to site. The only ferromagnetic material found to date that shows characteristics of random fields is the rare earth dipolar ferromagnet $LiHo_xY_{1-x}F_4$ [23]. As shown in Fig. 1.2, in the undoped material (x = 1), T_C is found to decrease gradually with increasing applied transverse field, $H_\perp$, as (1 - $H_\perp^2$), consistent with mean field theory (MFT). By contrast, dilution of the magnetic Ho ions with non-magnetic Y ions reveals a fundamentally different behavior. In particular, the material with x = 0.44 exhibits a much stronger, approximately linear, decrease of T_C with $H_\perp$. This has been attributed to the fact that a transverse field applied to a site-diluted ferromagnet leads to a random longitudinal field [24]. However, several factors have made it difficult to obtain unambiguous results in the case of $LiHo_xY_{1-x}F_4$. The two most important

are that dilution leads to randomness in the interactions themselves, and that the hyperfine fields are large and comparable to the dipole fields, further complicating the physics [25, 26].

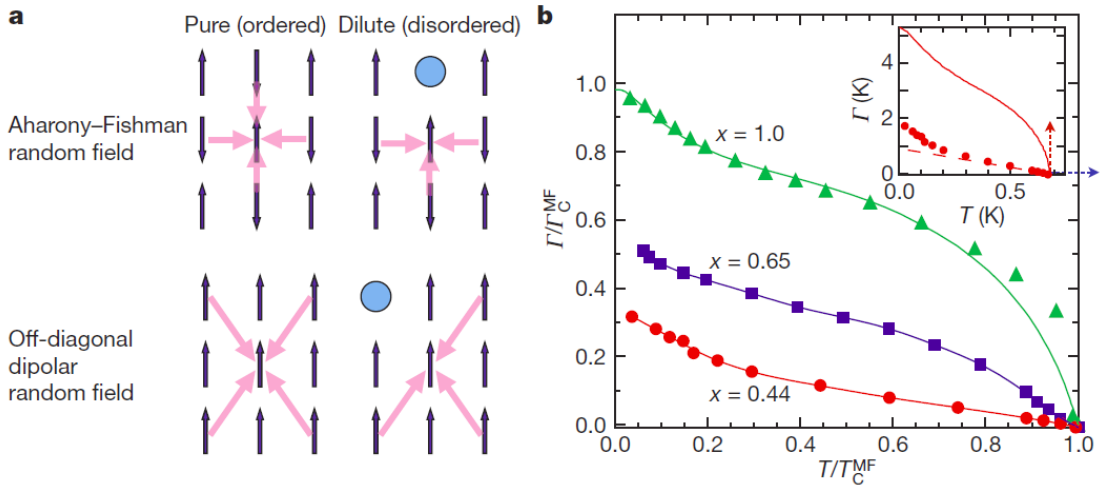

Figure 1.2: Fig. 1 of ref. [23]. Random fields in a diluted, dipolar-coupled ferromagnet drive the system away from mean-field behavior of a periodic system.

By contrast, the hyperfine fields are relatively unimportant in Mn_{12}-ac and there is no intentional dilution of the lattice so that the material is essentially a pure Ising ferromagnet with minimal disorder in zero field. Instead, the randomness arises from small tilts of the magnetic easy axis of individual molecules due to isomer disorder [27–31]: an applied transverse field has a nonvanishing projection along the local easy axis, leading to a random longitudinal field of scale set by the applied transverse field. Mn_{12}-ac and other single molecule magnets may therefore serve as clean model systems for the study of random field ferromagnetism where the random fields are controllable through an external transverse field, and considerably larger than typical hyperfine fields.

In this thesis, I will first review our experimental study of the temperature dependence of the magnetic susceptibility of Mn_{12}-ac as a function of transverse field, which leads to the proposal that a Mn_{12}-ac single crystal is a random field Ising

ferromagnet due to the isomer disorder.

This earlier study was carried out for several crystals using a single Hall sensor. The overall behavior was found to be the same, but yielded different Weiss intercepts. This was traced to the fact that demagnetizing field varies locally from point to point. A full calculation of the local demagnetization factor was executed, yielding a method for deducing the intrinsic susceptibility from measurements of the local susceptibility.

Then I will present a new experiment which utilized this data processing tool for a comparison study designed to demonstrate that the random field originates from the isomer disorder. Following our chemistry collaborator's (Prof. George Christou's) suggestion, we chose Mn_{12}-ac-MeOH (details will be given in Chapter 2), a SMM similar to Mn_{12}-ac in all respects except that it contains different solvent molecules of crystallization, which leads to the absence of isomer disorder and hence should not give rise to any random fields. The results for this variant, Mn_{12}-ac-MeOH, is consistent with the MFA calculation for a pure transverse field Ising ferromagnet, thus supporting our hypothesis that solvent disorder in Mn_{12}-ac induces the random field effect.

This thesis is organized in the following way:

Chapter 2 is an introduction to the relevant background information, including an introduction to Mn_{12}-ac and Mn_{12}-ac-MeOH, and a discussion of the solvent disorder in Mn_{12}-ac.

Chapter 3 is devoted to explaining the relevant experimental techniques. Compared to our earlier measurements, numerous technical improvements have been accomplished to achieve the later results. I will disclose all the important details to facilitate future follow-up studies.

Chapter 4 describes a study of the susceptibility of Mn_{12}-ac, and the random field model (RFIFM) that motivated the studies that followed.

Chapter 5 is devoted to a discussion of the demagnetization effect in the susceptibility measurements and how to correct the data for the demagnetization field.

Chapter 6 is focused on a comparison study of Mn_{12}-ac-MeOH, a clean system without randomness.

The thesis is summarized and concluded in chapter 7. Some suggestions for future research are also given.

Chapter 2

Background

2.1 Properties of Mn_{12}-ac and Mn_{12}-ac-MeOH

$[Mn_{12}O_{12}(O_2CMe)_{16}(H_2O)_4]\cdot 2MeCO_2H\cdot 4H_2O$, usually shortened as Mn_{12}-ac, is the first-synthesized and best-studied example of a SMM [32]. It crystallizes into a body centered tetragonal lattice (space group $I\bar{4}$), with unit cell parameters $a = b =$ 17.1668Å, $c = 12.2545$Å, number of molecules per unit cell Z=2, unit cell volume V = 3611.39 Å^3 at 83 K [33].

$[Mn_{12}O_{12}(O_2CMe)_{16}(MeOH)_4]\cdot MeOH$, referred to as Mn_{12}-ac-MeOH, is a new high symmetry derivative of Mn_{12}-ac. Similar to Mn_{12}-ac, Mn_{12}-ac-MeOH also crystallizes into a body center tetragonal lattice (space group $I\bar{4}$) with unit cell parameters $a = b = 17.3500$ Å, $c = 11.9971$ Å, $Z = 2, V = 3611.4$ Å^3 at -100 °C [34, 35].

Sample preparation for Mn_{12}-ac and Mn_{12}-ac-MeOH is described in Refs. [32] and [34, 35] respectively.

The magnetic core of Mn_{12}-ac-MeOH is the same as the original Mn_{12}-ac. As shown in Fig. 2.1, in both clusters, a central $Mn^{4+}{}_4O_4$ cubane (containing four Mn^{4+} (S=3/2) ions) is held within a nonplanar ring of eight Mn^{3+} (S=2) ions by eight μ_3-O^{2-} bridge ions. Four of the eight outer Mn^{3+}'s (labeled as Mn2) are each bridged to a Mn^{4+} by two μ_3-O^{2-} ions; the other four Mn^{3+}'s (labeled as Mn3) are each bridged to two Mn^{4+} ions by two μ_3-O^{2-} ions. This dodecanuclear cluster has S_4

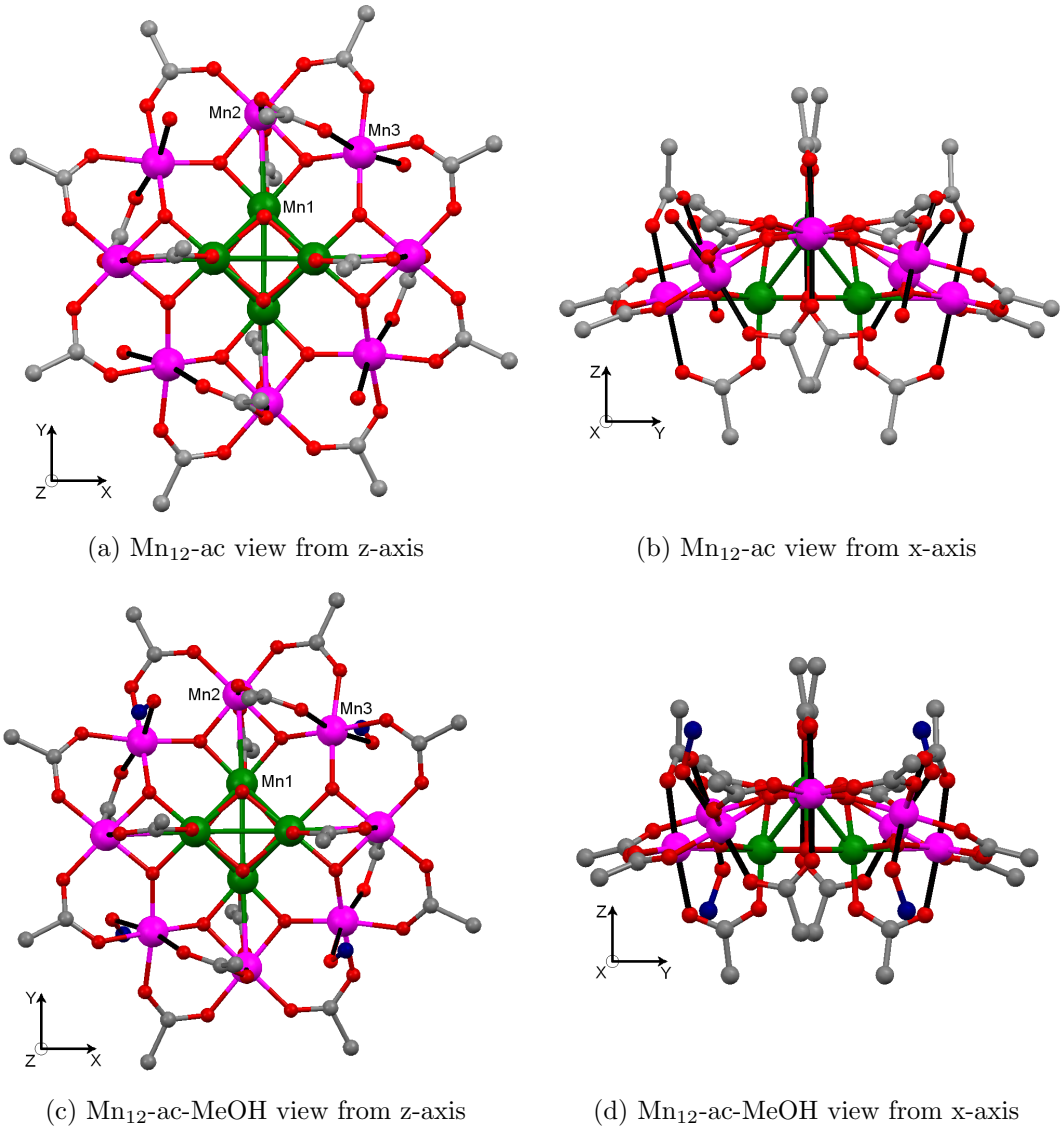

(a) Mn_{12}-ac view from z-axis

(b) Mn_{12}-ac view from x-axis

(c) Mn_{12}-ac-MeOH view from z-axis

(d) Mn_{12}-ac-MeOH view from x-axis

Figure 2.1: Molecule structure of the magnetic core $[Mn_{12}O_{12}(O_2CMe)_{16}(H_2O)_4]$ and $[Mn_{12}O_{12}(O_2CMe)_{16}(MeOH)_4]$; green balls are Mn^{4+} ions, purple balls are Mn^{3+} ions, red balls are oxygen, gray balls are carbon, hydrogen atoms are not displayed. The black bonds are the Jahn-Teller elongated axes which leads to the spin anisotropy. The blue balls in the Mn_{12}-ac-MeOH are the carbon atoms of the four terminal methanol molecules which substituted the terminal water molecules in the Mn_{12}-ac.

symmetry.

The Mn ions are coupled by superexchange interaction through the O bridge ions. The coupling nature of superexchange interaction depends on the angle. The angle of all the Mn^{4+}-(μ_3-O)-Mn^{3+} bonds are obtuse, thus the coupling between Mn^{4+} and

Mn^{3+} are antiferromagnetic, while the acute angle of the Mn^{4+}-(μ_3-O)-Mn^{4+} bond in the cubane keeps the four Mn^{4+} ions weakly ferromagnetically coupled. According to this scheme, the molecule would have an $S = (8 \times 2) - (4 \times 3/2) = 10$ ground state, which is confirmed by ac-susceptibility measurements [36–38] and EPR measurements [36, 37, 39–41].

Due to the symmetry, the molecule experiences a large anisotropy with easy axis along the z direction [36, 37, 42–44]. The magnetic properties can be understood by a spin Hamiltonian [45–49]:

$$\hat{\mathcal{H}} = -DS_z^2 - g_z\mu_B H_z \hat{S}_z + \hat{V}_T \tag{2.1}$$

where the coefficient D is the second order uniaxial anisotropy. For Mn_{12}-ac, the value of D has been reported to be from 0.548 K to 0.655 K [4, 5, 20, 29, 34, 50–52]; for Mn_{12}-ac-MeOH, $D = 0.667$ K [34]. This is usually modeled as a double well potential (Fig. 2.2).

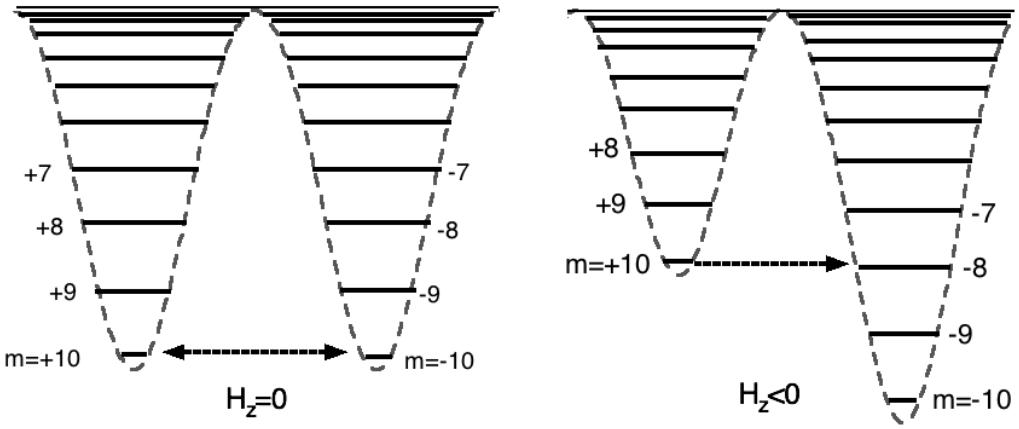

Figure 2.2: Double well potential of Mn_{12}

The $g_z\mu_B H_z \hat{S}_z$ represents the Zeeman interaction, and $g_z \approx 1.92$.

$\hat{V}_T$ is a small symmetry breaking term. In this thesis study, the dominant contribution to $\hat{V}_T$ is $g_x\mu_B H_T \hat{S}_x$, the transverse field term, for both systems. We will

show that a random field term, $g_z\mu_B H_{ran}(H_T)\hat{S}_z$, must be included in the Hamiltonian for Mn_{12}-ac.

2.2 Quantum tunneling of magnetization

One of the fascinating phenomena that SMMs exhibit is quantum tunneling of the magnetization, which can be observed in the hysteresis of magnetization curve.

At low temperature, the spins in SMMs do not have enough energy to climb over the double well potential energy barrier. The system relaxes slowly and stays in metastable state for a long time. The rate of relaxation to the true ground state is proportional to the probability of spins occupying the energy level at the top of the barrier. The magnetic relaxation time was found to follow an Arrhenius law: [36, 51]

$$\tau = \tau_0 e^{\triangle E/k_B T} \tag{2.2}$$

where $\triangle E/k_B = 61$ K and the prefactor $\tau_0 = 2.1 \times 10^{-7}$ s for Mn_{12}-ac. [51].

When the time scale of spin relaxation becomes longer than the external magnetic field sweep rate, hysteresis will be observed in the magnetization curve. It is worth pointing out that this is different from the hysteretic behavior of conventional ferromagnet, which originates from the slow relaxation entailing domain wall motion. Fig. 2.3a shows the magnetization of a Mn_{12}-ac single crystal for the case where the magnetic field is swept along the easy axis at 10 mT/s between 0.3 K and 3.0 K. The steps indicate that the magnetization is relaxing faster at certain fields (resonant fields) than at others, which was first observed and interpreted by Friedman *et al.* [4, 53] as evidence of quantum tunneling of magnetization, and later confirmed by many others [5, 6, 11, 54–56].

The interpretation is that at these so-called resonant fields, a pair of spin states are brought to the same energy by the external longitudinal magnetic field, providing a chance for the spins to tunnel through the energy barrier (Fig.2.3c). The quantum

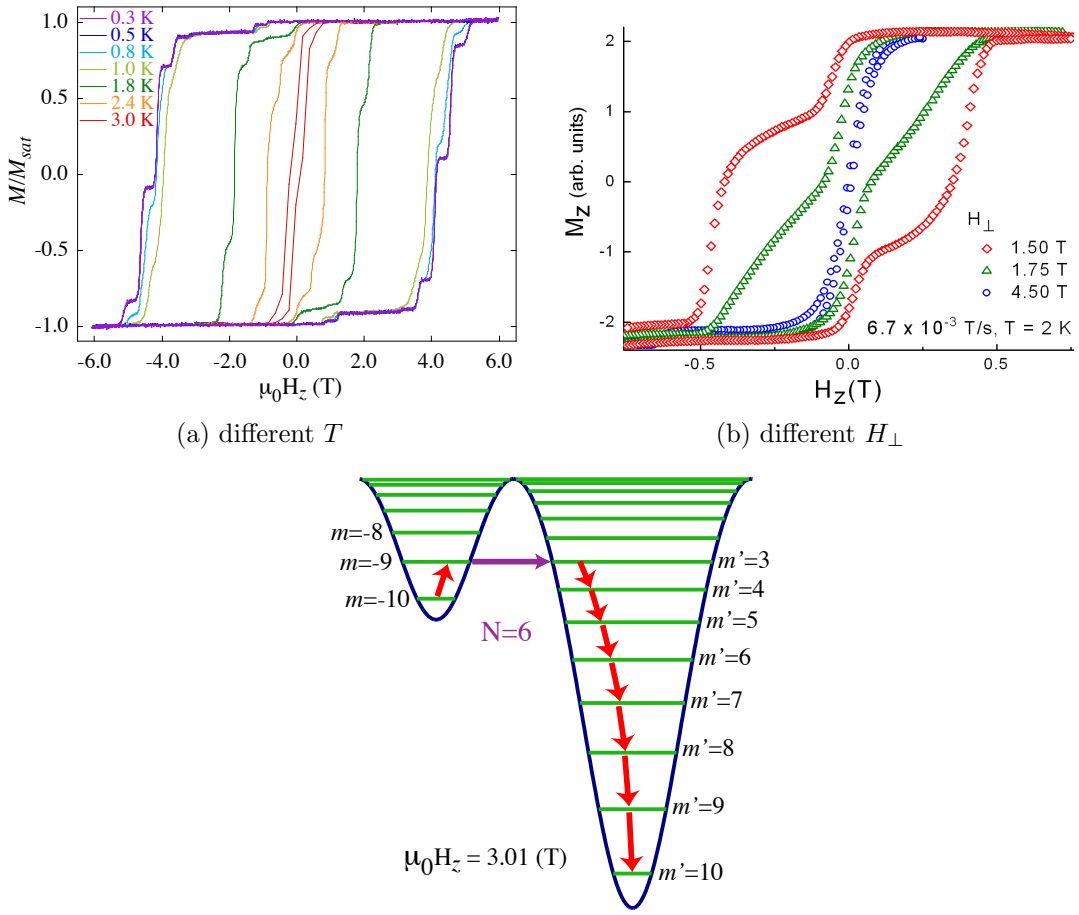

(a) different T

(b) different $H_\perp$

(c) resonant tunneling

Figure 2.3: Quantum tunneling of magnetization

tunneling provides the system an additional way to reach equilibrium, and thus promotes the spin relaxation. The quantum relaxation rate is determined by the tunneling oscillation frequency, which was first calculated by Garanin and Chudnovsky from the tunneling splitting Δ_m [57]:

$$\omega_m = \Delta_m/\hbar \tag{2.3}$$

A transverse magnetic field can promote the tunneling (see Fig. 2.3b) by increasing Δ_m [58]:

$$\Delta_m = \frac{2D}{[(-2m-1)!]^2}\frac{(S-m)!}{(S+m)!}\left(\frac{g\mu_B B_x}{2D}\right)^{2|m|} \tag{2.4}$$

2.3 Structural differences and isomer disorder.

Although Mn_{12}-ac and Mn_{12}-ac-MeOH are similar in many ways as described above, there are some crucial differences relevant to this study, which derive from the organic ligand and solvent molecules which form the local environment [34]. In Mn_{12}-ac-MeOH: (i) the four terminal water molecules in Mn_{12}-ac are replaced by terminal methanol molecules (CH_3OH, i.e., MeOH); (ii) the two acetic acid and four water solvent molecules in Mn_{12}-ac are replaced by only one methanol; and (iii) this methanol solvent molecule resides on a symmetry element, making the overall structure highly symmetric (crystallographic space group $I\bar{4}$).

As a direct result of (iii), the Mn_{12}-ac-MeOH crystal retains the molecular S_4 symmetry and thus should not contain any isomer disorder. In a perfect crystal, every molecule's easy axis (Ising axis, z-axis) lies along the crystal c-axis.

However, in Mn_{12}-ac, each molecule is surrounded by four acetic acid solvent molecules. Each acetic acid can form *only one* OH...O hydrogen-bond with the two Mn_{12} molecules it lies between. Thus each Mn_{12} molecule can have n (n=0-4) hydrogen-bonds around it, which results in six different isomers [27], and three different easy axis tilts (the molecule's z-axis forms an angle with the crystal c-axis). So although the core molecule itself has S_4 symmetry, the Mn_{12}-ac does not retain this symmetry in the crystal.

The relationship between the six isomers and easy axis tilts are illustrated below in Fig. 2.4:

a) For n=0 or n=4, the Mn_{12} molecule retains S_4 symmetry; for n=2 (trans) case, the Mn_{12} molecule has C_2 symmetry. In these three isomer cases, there are no easy axis tilts since the hydrogen-bonds' net effect in the x-y plane is zero under the high symmetry. (Fig. 2.4a)

b) For n=1 or n=3, the Mn_{12} molecule has only C_1 symmetry. The hydrogen-bonds

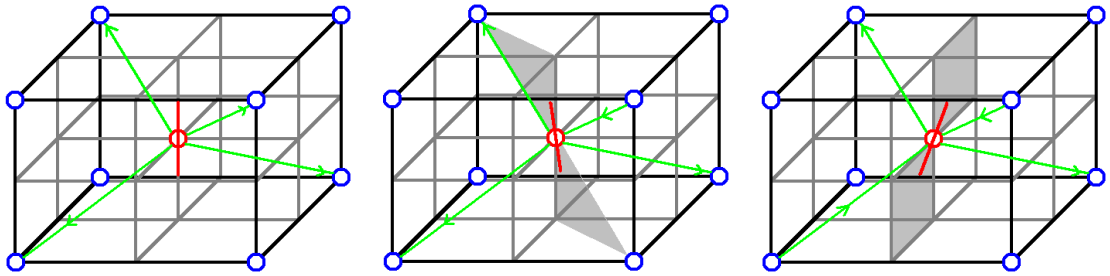

(a) n=0 case (b) n=1 case, φ=45° (c) n=2 (cis) case, φ=0°

Figure 2.4: Three examples of isomer tilts. Red ball is the molecule which we are exam. Blue balls are its nearest neighbors. Green arrows are the acetic acid solvent molecules with a hydrogen-bond on one side of it. Black and grey lines are just for perspective drawing.

will give a net effect pushing the easy axis to tilt towards one of the corners of the unit cell. Density functional calculations [31] predict a tilting angle θ around 0.5 degree; while HFEPR experiments [29] give results of approximately 1.5 degree. φ can be 45°, 135°, 225° or 315°. (Fig. 2.4b)

c) For the n=2 (cis) case, the easy axis will tilt towards one of the unit cell edge centers. θ is still 0.5 degree in theoretical calculations, around 1.5 degree in experiments. However, in this case, the value of φ falls into a set different from case b), namely it can be 0°, 90°, 180° or 270°. (Fig. 2.4c)

Fig. 2.5a gives a top view (looking along the z-axis) of the six isomers and the corresponding spin tilting directions. At first glance, the distribution of isomers in a Mn_{12}-ac crystal, as shown in Fig. 2.5b, seems to be random. But a closer analysi reveals that there are restrictions between the nearest neighbors, for example, it is impossible to have a pair of molecules as shown in the insert of Fig. 2.5a, as the acetic acid solvent molecule lying between them will be frustrated.

These restrictions will impose some short range correlations on the system, but whether these correlations will lead to observable long-range correlations, is a question outside the scope of this thesis and awaits future study. In this thesis, we ignore the nearest neighbor restriction and assume that all the isomer cases have equal

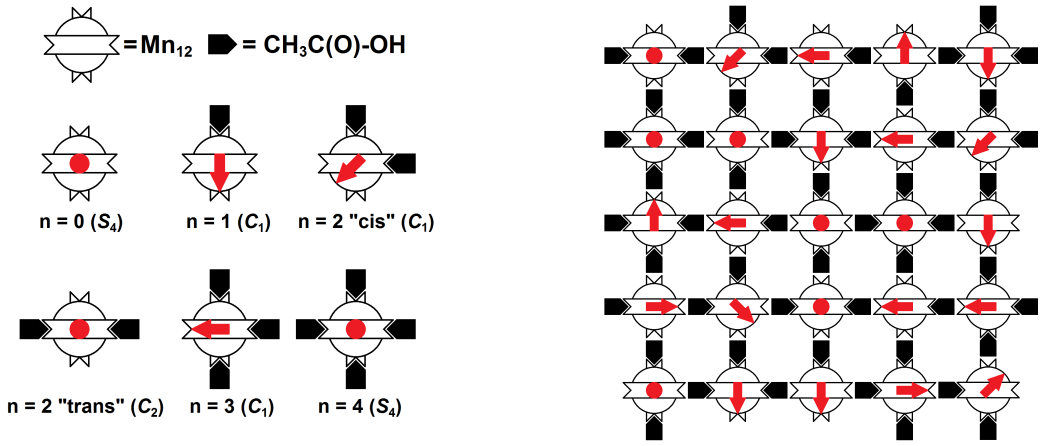

(a) (b)

Figure 2.5: (a) The six hydrogen-bond isomers of Mn_{12}-ac [59]; the red arrow indicates the spin tilting direction. (b) A schematic diagram of possible isomer distribution in the crystal; a real distribution is in three dimension and the bonds are lying between different layers.

probability. Thus the probability of the tilting angles are summarized in table 2.1. (The random field will be explained in Ch. 4. The information is included here for completeness)

i	1	2	3	4	5	6	7	8	9
θ_i	0	θ_0	θ_0	θ_0	θ_0	θ_0	θ_0	θ_0	θ_0
ϕ_i	0	0	$\pi/4$	$\pi/2$	$3\pi/4$	π	$5\pi/4$	$3\pi/2$	$7\pi/4$
h_i/h_{ran}	0	1	$1/\sqrt{2}$	0	$-1/\sqrt{2}$	-1	$-1/\sqrt{2}$	0	$1/\sqrt{2}$
P_i	1/4	1/8	1/16	1/8	1/16	1/8	1/16	1/8	1/16

Table 2.1: Table of values of polar θ and azimuthal ϕ angles along with the random field h_i (expressed as a fraction of $h_{ran} = g\mu_B H \sin\theta_0$ for field directed along crystal x axis) and probability of occurrence for isomer i host molecule in Mn_{12}-ac crystals.

2.4 Demagnetizing effect in magnetic measurements

A finite size specimen will be magnetized not only by the external applied magnetic field H_a, but also by H_d, the *demagnetizing field* generated by the induced magnetic poles in the specimen. The combined effect of these fields results in magnetization

$$\mathbf{M} = \chi(\mathbf{H_a} + \mathbf{H_d}), \tag{2.5}$$

where

$$\mathbf{H}_d = N \cdot \mathbf{M}. \tag{2.6}$$

The *demagnetizing factor*, N, is a function of the sample's shape and size [60,61]. The field, H_d, is directed opposite to the magnetization, while its intensity is proportional to the magnetization.

We need to determine the intrinsic property of the material, which does not depend on the specific specimen or particular experimental setup. However, the *demagnetizing effect* causes the magnetization measurement to depend on the specimen shape and size. Thus, in order to extract the intrinsic property of the material, the demagnetizing effect has to be taken into account when analyzing data. But, except for the ellipsoid-shape sample, the demagnetizing field in an arbitrary shape specimen is usually **nonuniform**. The spatial variation prevents us from defining a single demagnetizing factor.

The traditional way to deal with this problem is to define the demagnetizing factor as $\langle \vec{H}_d \rangle_{av} = N \cdot \langle \vec{M} \rangle_{av}$, where $\langle H_d \rangle_{av}$ and $\langle M \rangle_{av}$ are either averages over the mid-plane (measuring magnetization with a ballistic galvanometer), or over the entire volume of the specimen (measuring magnetization with a magnetometer). This approximation is only good when the demagnetizing field varies slowly in space, which usually requires that the sample have a high symmetry geometric shape and a smooth surface. However, for fragile materials, including the Mn_{12}-ac and Mn_{12}-ac-MeOH we studied in this thesis, the sample shape is not easy to control. If the sample has sharp corners or irregular surface, the demagnetizing field can have big fluctuations, in which case using an average demagnetizing factor cannot effectively correct the effects, and the error is large.

In Ref. [62], our group proposed a way to correct for the demagnetizing effect in global measurements of magnetization by measuring samples with different aspect ratio, and using the published relationship between demag factor and aspect ratio to

fit the data. In the end, we are able to extrapolate the Curie-Weiss temperature for an infinitely long sample, for which the demagnetization field is zero, as shown in Fig. 2.6.

In local magnetic measurements, such as Hall magnetometry measurements, the problem becomes more complicated as the demagnetizing fields are location-dependent. We will show in Ch. 5, that as a result of the demagnetizing field, the measured/apparent susceptibility may change by as much as a factor of three between two sensors with a 200 μm spacing. This can further lead to 40% changes in the Curie temperature deduced from the inverse susceptibility versus temperature. Then a magnetostatics calculation is performed to simulate the Hall measurements, in order to investigate the effect of different experimental factors on the measurement result.

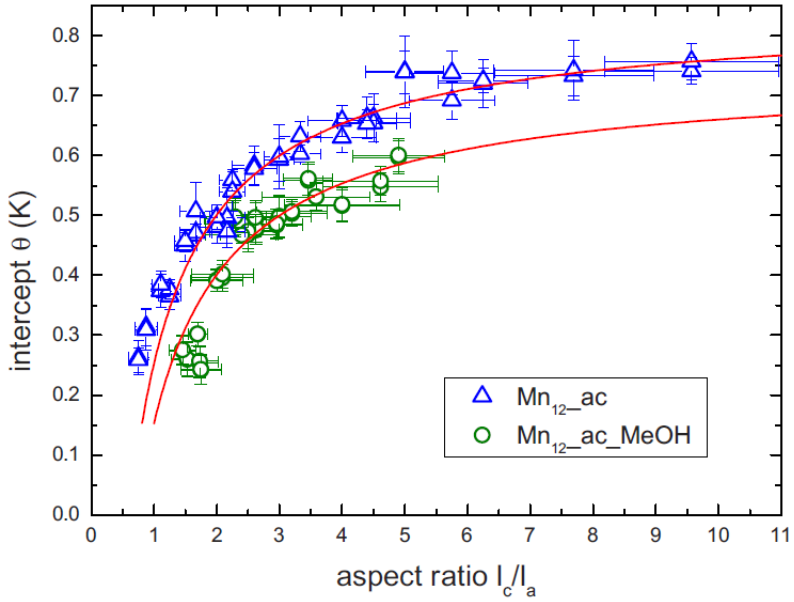

(a) (FIG. 3. from Ref. [62])

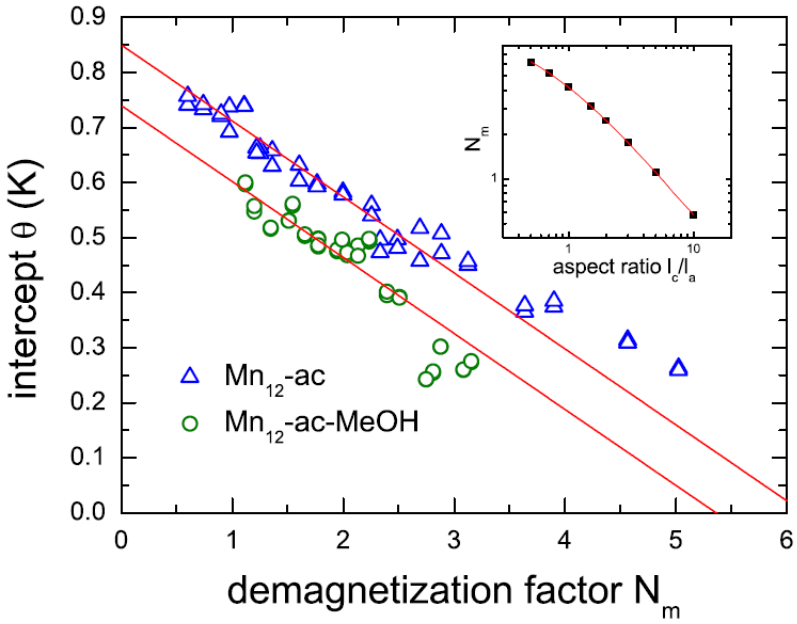

(b) (FIG. 4. from Ref. [62])

Figure 2.6: (a) Temperature intercept θ as a function of aspect ratio for Mn_{12}-ac (triangles) and Mn_{12}-ac-MeOH (circles). The lines denote fits obtained as described in Ref. [62]. (b) Temperature intercept θ as a function of demagnetization factor N_m (in cgs units) for Mn_{12}-ac (triangles) and Mn_{12}-ac-MeOH (circles). Approximate fits are denoted by the solid lines with (negative) slopes constrained to be equal to the Curie constant $C = 0.138$ [see Eq.(1) in Ref. [62]]. Inset: magnetometric demagnetization factor N_m as a function of aspect ratio; values of N_m are obtained by interpolation from the tables published by Chen, Pardo and Sanchez (Refs. [63, 64]).

Chapter 3

Experimental procedure

3.1 Samples

More than twenty single crystals were studied. They were prepared by students (C. Lampropoulos and S. Mukherjee) from Prof. G. Christou's group in University of Florida [32, 35, 65]. Six of them were studied thoroughly and the data will be presented in this thesis:

Mn_{12}-ac:

Sample A, dimensions $\sim 0.4 \times 0.4 \times 2.17$ mm^3;

Sample B [20, 66], dimensions $\sim 0.4 \times 0.4 \times 2.4$ mm^3;

and Sample C, dimensions $\sim 0.3 \times 0.3 \times 1.85$ mm^3.

Mn_{12}-ac-MeOH:

Sample D [66], dimensions $\sim 0.2 \times 0.2 \times 0.95$ mm^3;

Sample E, dimensions $\sim 0.085 \times 0.085 \times 0.68$ mm^3;

and Sample F [67], dimensions $\sim 0.075 \times 0.075 \times 0.85$ mm^3.

3.2 Instrumentation

All the measurements were performed between 0.5 K and 20 K in a commercial Oxford Heliox 2^{VL} sorption-pumping ^{3}He refrigerator, inserted into an American Magnetics, Inc.'s LN_2 shielded Helium research dewar with a built-in 3-Axis superconducting

magnet. The vector magnet consists of an 8 T solenoid with its axis in the vertical direction and two Helmholtz coils in the horizontal plane generating up to 1 T and 0.7 T respectively.

For samples A, B, D, data were taken by a single GaAs/GaAlAs Hall sensor made by a previous NYU student, Gregoire De LOUBENS. The sensor has an active area of $50 \times 50\ \mu\text{m}^2$. It was placed near the edge of the crystal, where the measured B_x is assumed to be a linear function of M_z (see section 3.3 and Ch. 5 for detailed discussions). Care was taken to align the sample and the Hall bar (placed in the y-z plane) relative to each other and relative to the applied magnet field as shown in Fig. 5.2

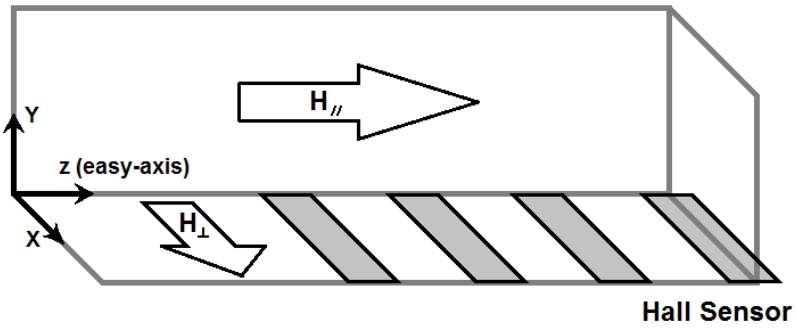

Figure 3.1: A schematic diagram of the experimental setup. For samples A, B, D, we used only the single sensor on the edge of the crystal. For samples C, E, F, we used multiple sensors in an 1D array.

For the experiments with samples C, E, F, we used an improved setup. First, a homemade chip holder was designed and made from a Copper-Clad PCB, as shown in Fig. 3.2. Second, the Hall sensor was replaced by a Hall sensor array, which was made by Pradeep Subedi and me from a new GaAs/GaAlAs heterostructure wafer. The design details of this Hall sensor array will be given in the next section 3.3. Third, to improve the thermal conduction for more accurate temperature measurement, a piece of copper plate was left on the chip holder to function as a heat sink. The sensor wafer was glued on the heat sink by MG Chemicals® Pure Silver Conductive

Epoxy (Cat. No: 8331). A Lakeshore Cernox^{TM} cryogenic temperature sensor and a Lakeshore Ruthenium oxide (ROX^{TM}) temperature sensor were glued on the heat sink by GE-varnish. The Cernox thermometer was used to provide an accurate temperature reading at zero magnetic field. The ROX thermometer is designed to give low magnetic field-induced errors. Thus we used it to monitor the temperature drift in finite magnetic field. Fourth, a piece of copper braid (taken from a solder wick) was used to transfer the heat to the cold finger. One end was glued by GE-varnish then bolted on the heat sink, the other end was fixed on the cold finger in a similar way. See Fig. 3.2 for details.

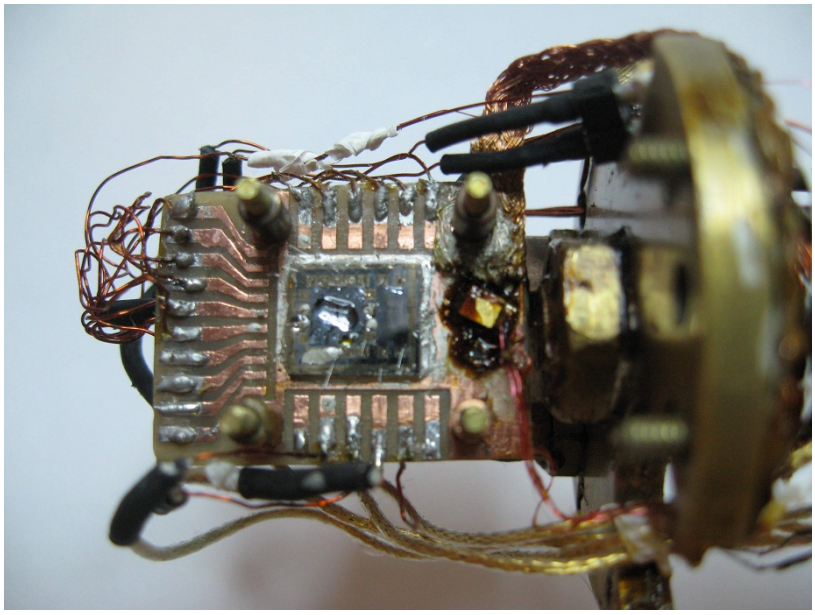

Figure 3.2: A photo of the improved experiment setup.

3.3 Hall magnetometry

Hall magnetometry uses the classical Hall effect to detect the magnetic field. The classical Hall effect was discovered by Edwin Hall in 1879 [68]: a voltage difference appears across an electrical conductor, transverse to the current flow when a magnetic field is applied perpendicular to the current.

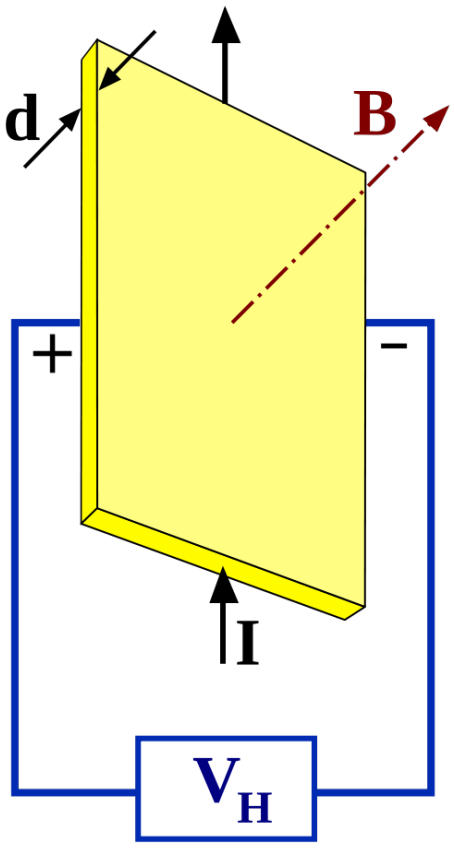

(a) A schematic diagram of a Hall magnetometer (picture belongs to Wikipedia).

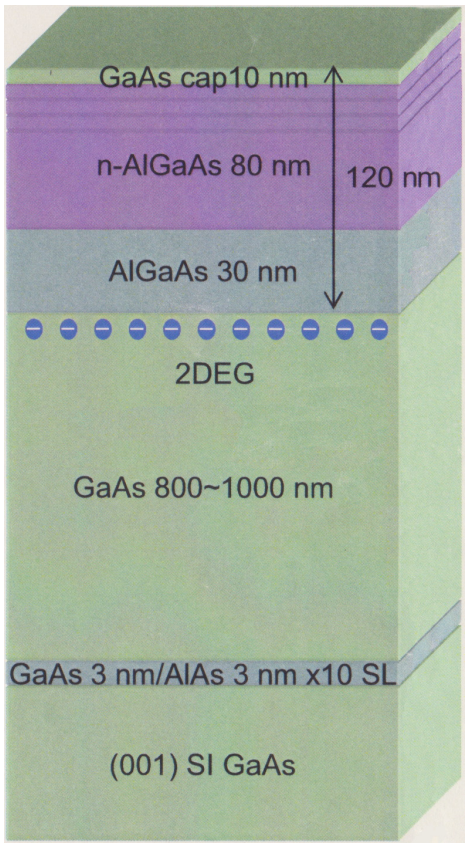

(b) Structure of the GaAs/GaAlAs wafer

Figure 3.3

A Hall magnetometer will show a voltage:

$$V_H = \frac{R_H}{d} IB \tag{3.1}$$

where $R_H = \frac{1}{nQ}$ is the Hall coefficient of the device (n is the charge carrier density, Q is the charge of the carriers with sign).

For a 3D device, the thickness d will affect the result. But in this study, we used a GaAs/GaAlAs quantum well Hall sensor, which is a 2DEG (two dimensional electron gases) system. The Eq. 3.1 can be rewritten with 2D sheet carrier density

$n_{2D} = n \times d$, and electron charge $Q = -e$:

$$V_H = -\frac{IB}{n_{2D}e} \tag{3.2}$$

The GaAs/GaAlAs semiconductor wafer is provided by our collaborator Yuzo Ohno from Riec Tohoku University. The structure is shown in Fig. 3.3b.

3.3.1 Hall array design

In order to study how the magnetization varies along a sample, we need a device which can measure the magnetization at different locations along the sample at the same time - we used a one dimensional array of Hall sensors.

Fig. 3.4 shows the photolithography mask of the Hall array, which produced the devices we used in Ch. 5 and Ch. 6. The active area is 20×100 μm^2. The distance between neighboring sensors is 200 μm. This design suits our measurement needs: Compared to the typical crystal size (Mn_{12}-ac is $\sim 0.3 \times 0.3 \times 1.5$ mm^3, Mn_{12}-ac-MeOH is $\sim 0.15 \times 0.15 \times 1$ mm^3), the sensor size is small enough to probe local information while still providing a good signal to noise ratio; the neighbor distance provides good coverage along the whole crystal to take measurements of different parts.

3.3.2 Background subtraction

In reality, due to flux trapping and non-ideal wiring, the field generated by the superconducting magnet is not strictly uniform in space. Although the external fields (both the the longitudinal field in z direction and transverse field in x direction) are applied **parallel** to the Hall sensor surface as shown in Fig. 5.2, the Hall sensor will still pickup some signal due to the non-uniformity. In order to remove this background from the signal, we need a Hall sensor to monitor the background signal.

There are two considerations in design:

1. The background sensor's surface has to be exactly parallel with the real signal sensor's surface in order to detect the same background.

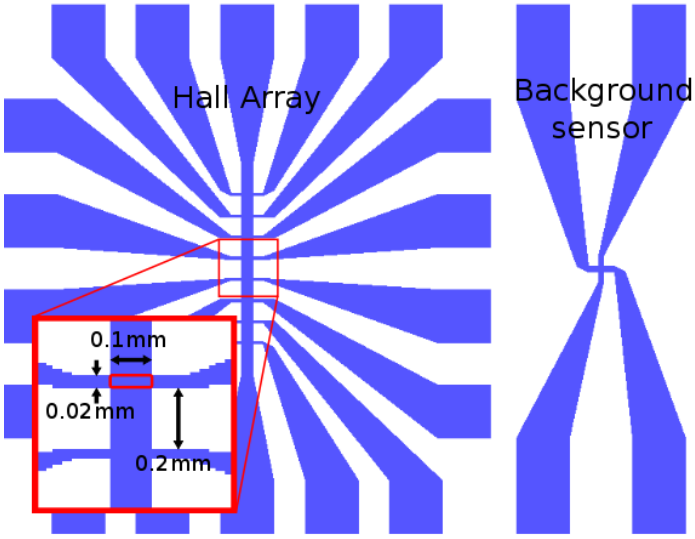

Figure 3.4: Photolithography mask of Hall array and background sensor.

2. The background sensor has to be close enough to the real signal sensor while not too close to pick up the sample signal.

The first requirement can be achieved by integrating the background sensor and sample sensor on the same semiconductor wafer. Our Hall sensor's senses via 2DEGS that exists on the interface of GaAs layer and AlGaAs layer, which is flat at an atomic level. This ensures that the background sensor and the Hall sensor will measure the same magnetic field component.

The second requirement is achieved empirically. First, we arranged the background sensor to be on the side of the array rather than on the top or bottom, such that when the sample is placed along the array, it won't be pointing towards the background sensor. Second, the distance between the background sensor and the Hall array is about 3 mm. Compared with the typical width of the sample ($\sim$ 0.3 mm), this distance should prevent the background sensor from picking up the signal from the sample.

The effect of subtracting the background sensor signal from the sample sensor signal is shown in Fig. 3.5. The result is satisfactory.

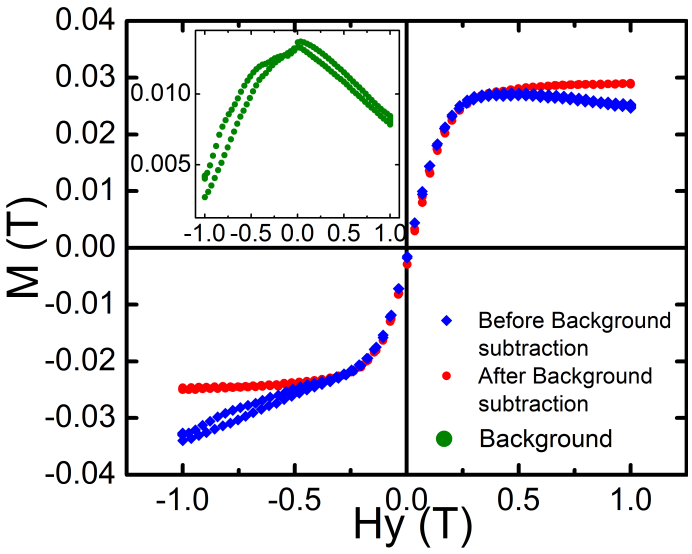

Figure 3.5: Subtracting background signal.

3.4 Equilibrium measurements

In our susceptibility study, we need to perform the measurements in equilibrium, because the Curie-Weiss applies to a system in equilibrium. The longitudinal field sweep rate α, the temperature and the transverse field, are three factors that determine whether the measurement is taken at equilibrium. However, T and $H_\perp$ are also parameters controlling the susceptibility, which will be predetermined for each experiment. Thus, for a given set (T, $H_\perp$) the longitudinal field sweep rate is the only free parameter that can be adjusted to reach equilibrium.

As mentioned before in Sec.2.2, for a given $H_\perp$, the relaxation time τ gets longer as the temperature gets lower. On the other hand, the transverse magnetic field can promote quantum tunneling. As the $H_\perp$ increases, the relaxation time τ will become shorter.

To stay in quasi-equilibrium, we need to keep the longitudinal field sweep rate α slow enough so that the experimental time scale stays larger than τ. Otherwise, the longitudinal magnetization of Mn_{12}-ac exhibits hysteresis due to slow spin reversal

and steps in the magnetic hysteresis loops due to quantum tunneling between opposite spin projections (Fig. 2.3) [4].

We define the blocking temperature, T_B, as the critical temperature point above which the system stays in equilibrium for a given sweep rate at a certain transverse field. We determined the boundary between the blocked and unblocked states for Mn_{12}-acetate shown in Fig. 3.6.

The effect of reducing α is demonstrated in the two insets of Fig. 3.6, which show the hysteresis loops obtained for three different sweep rates of longitudinal magnetic field in a narrow range ± 0.01 T about $H_z = 0$, measured in the presence of a constant transverse field $H_\perp = 2$ T at $T = 2.15$ K and $T = 2.40$ K. The point $H_z = 0$ was determined by symmetry from full magnetization curves taken between -1 and 1 T (see Fig. 2.3). In each case, hysteresis is observed at the faster sweep rate indicating that the system is below the blocking temperature; at the slower sweep rate the hysteresis loop is closed, indicating the system is above the blocking temperature and equilibrium is reached.

The applied transverse field $H_\perp$ accelerates the relaxation of the magnetization towards equilibrium, lowering the blocking temperature, T_B, as expected. Note that a reduction in T_B is also expected from a classical model of single domain uniaxial nanomagnets – the classical version of Mn_{12}-ac – where $T_B = (1 - h)^2$, $h = H/H_A$, H is the externally applied transverse field and H_A is the anisotropy field ($H_A = 2DS/g\mu_B \approx 10$ T) [69]. The solid line in Figure 3.6 is a fit of the measured T_B to the predicted quadratic dependence on field.

For the magnetization measurements from which we deduced the susceptibility, we always ascertained that the sample was in the unblocked phase, i.e., in equilibrium.

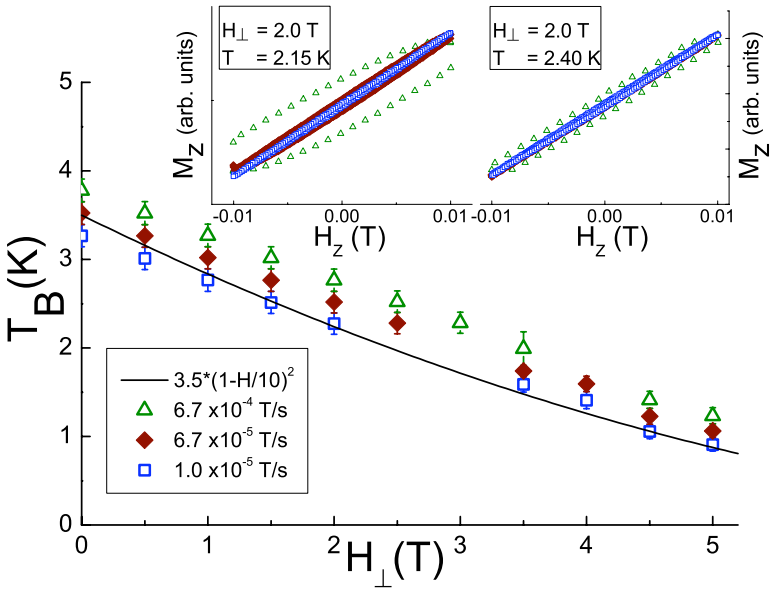

Figure 3.6: Blocking temperature versus $H_\perp$ for three different longitudinal field sweep rates (experimental time scales) in Mn_{12}-acetate. a. Magnetization as a function of the longitudinal field swept at the indicated rates for $H_\perp = 2$ T at $T = 2.15$ K and $T = 2.40$ K. b. Blocking temperatures for three longitudinal field sweep rates as a function of $H_\perp$.

3.5 Other techniques

3.5.1 Microscopy

We have used several different ways to take microscope pictures.

The Olympus BX60M microscope has a very high magnification. It is very useful for taking pictures of the fine details of the crystal (see Fig. 3.7). However, the view is too restricted for getting a whole picture of bigger objects, like the whole Hall sensor device.

In most circumstances, we used a normal point-and-shoot digital camera to take pictures directly from the eyepiece on a optical microscope (Fig. 3.8). This garage-style method turned out to be the best in practice. First, the camera can take pictures from any optical microscope. So the magnification is not restricted. Second, the photo quality is controlled by the camera, better picture quality can be achieved

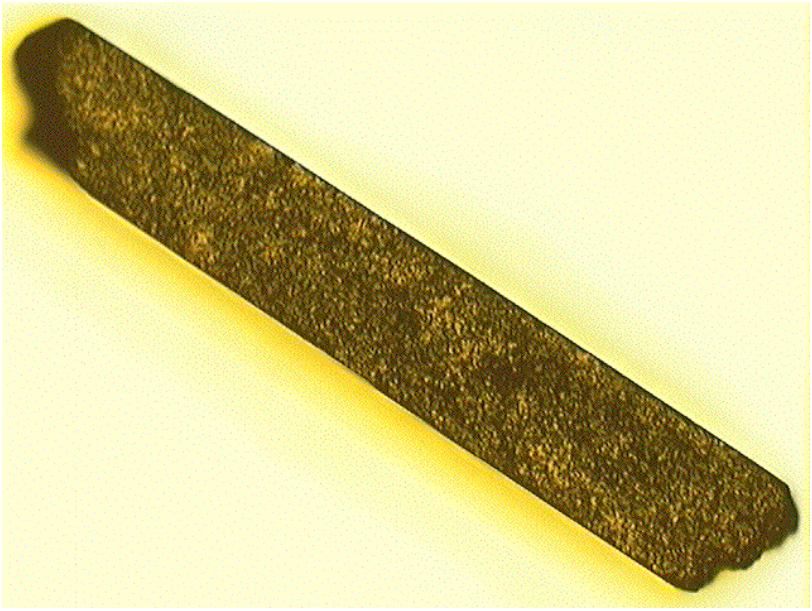

Figure 3.7: BX60M microscope image of Mn_{12}-acetate.

with a better camera. Third and most importantly, we can document important steps during mounting the sample, adjusting the crystal position and etc. directly on the working station, without moving the whole setup to the BX60M.

(a) (b) (c)

Figure 3.8: documenting experiment setup with point-and-shoot digital camera

3.5.2 Measurement of crystal geometry and position

In order to measure the size of the crystal, we took photos of the crystal on a microscope scale, as shown in Fig. 3.9. Usually we took photos of all four surfaces of the crystal, and later by examining the photos on a computer, we were able to determine the geometric information of the crystal.

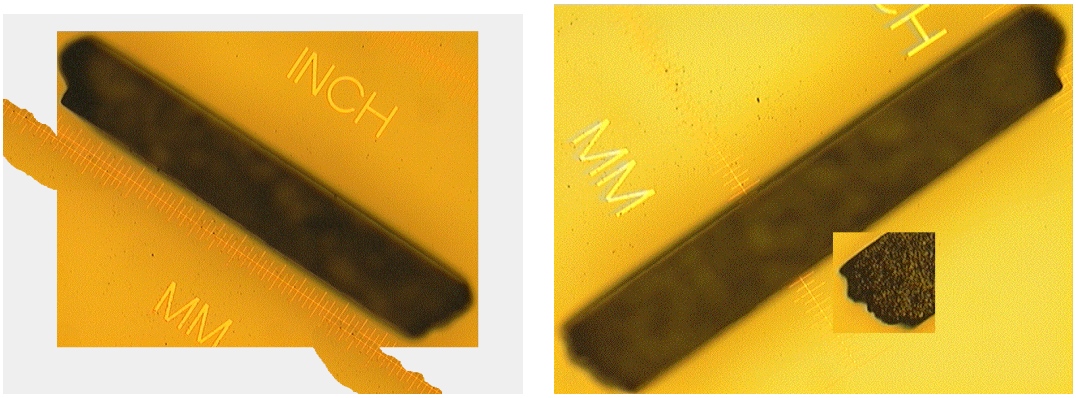

(a) (b)

Figure 3.9: Microscope photos taken for crystal measuring.

By combining the microscope photo of the crystal with that same crystal on the Hall sensor and the Hall sensor's photolithography mask shown in Fig. 3.10, we were able to determine the crystal's position relative to the Hall sensor.

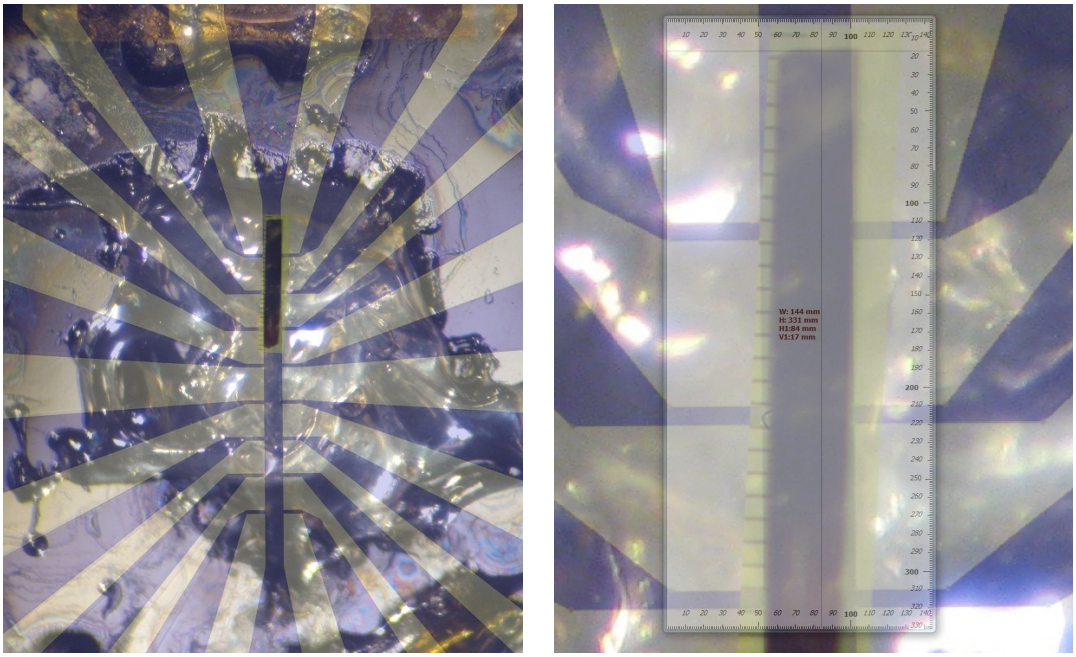

(a) (b)

Figure 3.10: Measurement of crystal positioning on Hall sensor.

3.5.3 Crystal handling of Mn_{12}-ac

In this study, we are interested in the magnetic behavior of the crystal in a transverse field. A magnetized sample experiences a mechanical torque in this transverse field, which was large and often caused the sample to break and fly off the sensor.

After about twenty times of trial and error, we developed the following procedure to position the Mn_{12}-ac crystal: First, we coat the crystal with a thin layer of DOW CORNING high vacuum grease (silicon base) to protect it from other corrosive chemicals. Second, we place the greased crystal on a glass slice which is also coated with vacuum grease. Third, we carefully put a suitable amount of STYCAST 1266 epoxy over the crystal and let it cure for 24 hours. Fourth, we transfer the encased crystal onto the Hall sensor and align them properly (the STYCAST 1266 is transparent so that we can see through it). Fifth, we use a syringe to apply a little amount of thinned GE-Vanish, so that it will fix the encased crystal on the Hall sensor without applying stress and moving the sample during drying. Then we repeat the fifth step several times until enough GE-Vanish has been applied so that the crystal is secured onto the Hall sensor surface firmly.

The reason for this complicated procedure is the following:

1) The vacuum grease does not provide enough grabbing force on the Hall sensor surface to balance out the torque, so that we need to use stronger glue like GE-varnish.

2) The GE-varnish and epoxy is corrosive to the Mn_{12}-ac crystal. They cannot be applied directly to the sample. We need to cover the crystal with a vacuum grease.

2a) We experienced several times that the crystal broke into pieces after cooling when we glued the crystal with only GE-varnish. Then we found out that the common solvent of GE-varnish is a 1:1 solution of Toluene and Ethanol, and Ethanol dissolves the Mn_{12}-ac crystal. Fig. 3.11a shows the Mn_{12}-ac stored in different common chemicals for one week. The crystal in Ethanol was completely dissolved.

2b) Aliphatic Amine is curing agent of STYCAST 1266 epoxy. It seems that

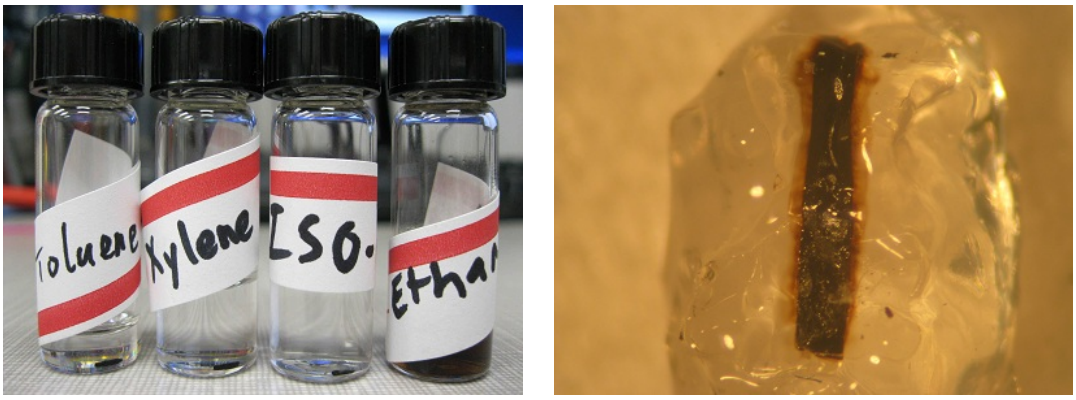

(a) Mn_{12}-ac in different chemicals

(b) Mn_{12}-ac dissolved in epoxy (by curing agent)

Figure 3.11: Crystal mishandling

its strong oxidization ability will likely to react with Mn_{12}-ac, changing the surface property. We saw that the crystal's surface looked as if dissolved after it was encased in STYCAST 1266 (Fig. 3.11b).

3) Although GE-varnish and vacuum grease should have been hardened after cool down, we found that they were not strong enough against the magnetic force. One time the crystal was crosscut into half: the bottom was still glued on the surface, but the top half was broken off and flew away. We chose to embed the crystal in a block of STYCAST 1266 epoxy, which was able to provide enough mechanical strength. To summarize, the purpose of the epoxy is to improve the mechanical strength to prevent the crystal breaking into small parts in high field; the purpose of the GE-Vanish is to act as an adhesive to fix the sample on the Hall sensor; the purpose of the vacuum grease is to protect the crystal from the Aliphatic Amine in the epoxy curing agent.

3.5.4 Crystal handling of Mn_{12}-ac-MeOH

The procedure for Mn_{12}-ac-MeOH crystal is different. The crystals have to be stored in the mother liquor, because the solvent molecule in these crystals has an evaporation temperature lower than room temperature, i.e., the crystal will lose the solvent

molecule and dissolve at room temperature when exposed to vacuum or atmosphere. Following our chemistry collaborator's suggestion, the samples were coated with Paratone® N to prevent degradation by crystal lattice dissolving [34]. Because the size of the Mn_{12}-ac-MeOH crystal is small compared to the Mn_{12}-ac crystal, the magnetic torque is also smaller. It was enough to hold down the sample on the Hall sensor in transverse field up to 5.5T by covering the Paratone N coated crystal with vacuum grease.

Chapter 4

Random field Ising ferromagnetism in Mn_{12}-ac

In this chapter we review our earlier findings for the usual form of Mn_{12}-ac. Interacting Ising spins that preferentially orient either "up" or "down" form a basis for understanding a broad range of complex natural phenomena. Long ranged order competes with thermal and quantum spin fluctuations and with the randomness which is present in any real material. A fundamental model used to study the interplay between these effects is the transverse field Ising model in a random magnetic field [70–72].

In this chapter we report a study of single crystal Mn_{12}-ac as an experimental realization of a system with tunable random magnetic fields. Slow spin relaxation and hysteresis preclude measurements of equilibrium properties at the low temperatures at which magnetic ordering occurs. Our approach is, therefore, to deduce the nature of the magnetic interactions from measurements of the magnetic susceptibility at temperatures above the blocking temperature.

4.1 Measurements

Using the setup we described in Ch. 3, measurements were performed on two Mn_{12}-ac single crystals (sample A, dimensions $\sim 0.4\times0.4\times2.17$ mm^3 and sample B, dimensions $\sim$ 0.4 × 0.4 × 2.4 mm^3). Data are shown for sample B; sample A displays the

same qualitative behavior but the inverse susceptibility showed a lower temperature intercept of 0.5 K in zero transverse field due to the demag effect (see Ch. 5 for more discussion). Measurements were taken between 0.7 K and 5.5 K. A longitudinal field, H_z, was swept along the sample's easy axis at rates between 1×10^{-5} T/s and 6.7×10^{-4} T/s, in the presence of a constant transverse field $H_\perp$ (up to 5 T) applied in the x direction.

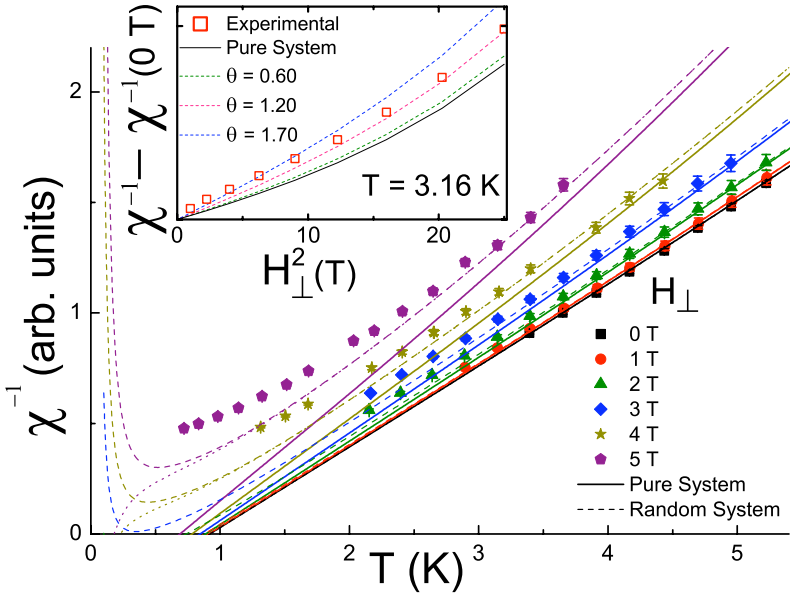

Figure 4.1: Temperature and field dependence of the inverse susceptibility of Mn_{12}-ac. Main panel: Filled symbols denote the inverse susceptibility of a single crystal of Mn_{12}-ac as a function of temperature in different transverse fields $H_\perp$ as labeled. The solid lines are the result of mean field calculations for a hypothetical system with no tilts. The dashed lines are obtained from mean field calculations incorporating the effects of random tilt angles, as discussed in section IV-B of the main text with root mean square tilt angle 1.2°. The dotted lines present theoretical results for a different distribution with the same mean square tilt angle but in which 25% of the sites are not tilted. Inset: Symbols represent the difference $[\chi^{-1}(H_\perp) - \chi^{-1}(H_\perp = 0)]$ versus $H_\perp^2$. The dashed, dotted and dash-dotted lines are calculated using the model of Section IV-B but with different root mean square tilt angles as indicated. The solid line displays results for the pure case.

Figure 4.1 shows the experimental results presented in this chapter: the measured equilibrium longitudinal susceptibility of a Mn_{12}-ac single crystal plotted as its inverse versus temperature and applied transverse field. As noted, these measurements were

performed at temperatures above $T_B(H_\perp, \alpha)$, i.e. in equilibrium condition (see Sec. 3.4 for details). The longitudinal magnetic susceptibility, $\chi = \partial M_z/\partial H_z|_{H_\perp=0}$, was deduced from the slope of the reversible M_z versus H_z at $H_z = 0$. The solid symbols in Fig. 4.1 show the inverse of the longitudinal susceptibility as a function of temperature for transverse fields between zero and 5 T. For zero transverse field χ^{-1} obeys the Curie-Weiss law expected from mean field theory (MFT), $\chi^{-1} \sim (T - T_{CW})$. The black line is a fit of the data in zero transverse field to a Curie-Weiss form; the extrapolated intercept $T_{CW} \sim 0.9$ K implies a transition at this temperature from paramagnetism (PM) to ferromagnetism (FM), consistent with the result of Luis *et al.* [16]. As $H_\perp$ is increased from zero, there is a systematic increase in the inverse susceptibility, accompanied by a progressively larger deviation from the straight-line behavior found at $H_\perp = 0$. Contrary to our expectation, this behavior is not consistent with mean field theory for a transverse field Ising ferromagnet. Further thought and a search of the literature revealed that there is a similarity between our data and data for the LiHoY system, which was attributed to the effect of random field. The detailed theory is presented in the next section.

4.2 Comparison with theory

4.2.1 Randomness in Mn_{12}-ac

While the susceptibility of Mn_{12}-ac in small transverse fields is well described by mean field theory using a Hamiltonian for a well-ordered "pure" system, it is clear that this model fails to describe the data obtained in the presence of a large transverse field, indicating the presence of physics not included in the pure-system calculation. We suggested that the additional physics is a random-field effect arising from structural disorder in the Mn_{12}-ac crystal [27,30,59]. In particular, different isomers of the host acetate material have been shown [73] to cause the spin quantization axis of some of the Mn_{12}-ac molecules to tilt away from the crystal z-axis by a small monomer-dependent

angle θ (see Sec. 2.3 for more details). As illustrated schematically in Fig. 4.2, on sites with a non-zero tilt angle a magnetic field applied transverse to the crystal z-axis has a component directed along the spin quantization axis; these longitudinal components are randomly distributed, and their magnitude is controlled by the size of the externally applied transverse field.

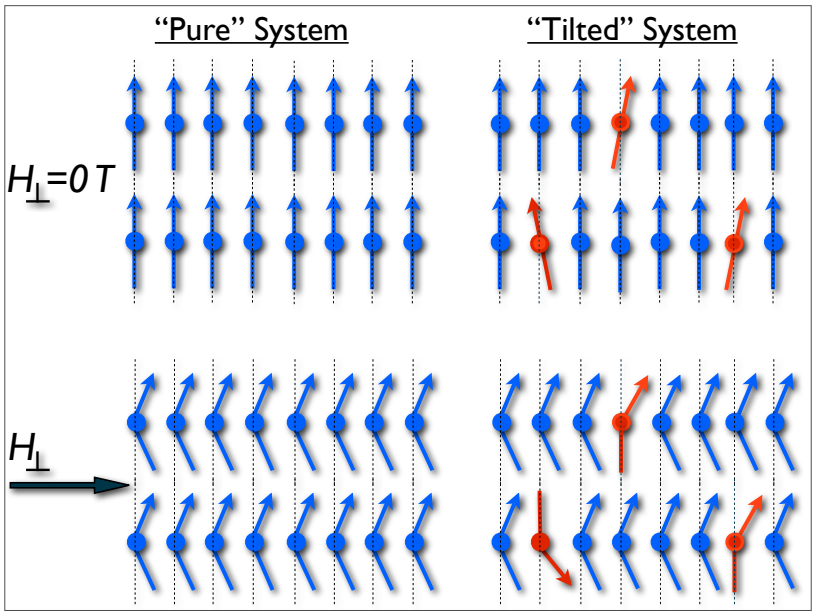

Figure 4.2: Effect of easy axis tilts on the transition temperature. In zero field a perfectly ordered crystal and a crystal in which there are easy axis tilts (e.g., the red spins) will order at nearly the same temperature (the small tilts do not greatly modify the interaction between spins, which depends on the longitudinal component of the magnetic moment). In an applied transverse field, the spins of misaligned molecules experience a field along their Ising axis. When this field is comparable to the exchange field these spins are frozen (red spins) and do not order. This leads to an effective dilution of the spins, a decrease in the susceptibility and a reduction in the transition temperature. It also increases the random field on the other sites in the crystal.

4.2.2 Theoretical Results and Comparison to Data

Millis *et al.* [21] introduced a theoretical model using mean field theory (MFT) to calculate the inverse magnetic susceptibility χ^{-1} with the random-field effect taken into account. First, the χ^{-1} contains two parts: $\chi^{-1} = \chi_{mol}^{-1} - J$, where χ_{mol}^{-1} is the

susceptibility of a single molecule, which can be calculated from the single molecule Hamiltonian H_{mol}, and J is the intersite dipole interaction which can be obtained on the lattice appropriate to Mn_{12}-ac. For the detail of the calculation, please refer to Ref. [21].

The solid lines shown in Fig. 4.1 are the result of calculations for the pure system without randomness. As $H_\perp$ is increased, the slope of the calculated traces increases, reflecting spin canting induced by the magnetic field. Also, due to the increase in quantum tunneling, the estimated ferromagnetic transition temperature (the extrapolated value where χ^{-1} vanishes) decreases and the calculated traces develop a weak curvature at low temperatures. The pure-system calculation and the data agree well only at small transverse fields.

The dashed lines in Fig. 4.1 show the results of calculations that include the randomness associated with isomer tilts. Here we have assumed that all the sites have a tilt and the mean square tilt angle is 1.2°, larger than the 0.4° calculated by Park *et al.* [73] but in good accord with the values determined using EPR [29] (which finds tilts up to 1.7°). Although not in complete agreement with the data, the theory with randomness accounts for all the major features of the observed $\chi^{-1}(T)$ in transverse fields.

The inset of Figure 4.1 compares the measured and calculated field dependence of χ^{-1} at a fixed temperature (3.16 K). The quadratic field dependence at low fields follows from general principles. The magnitude is seen to be inconsistent with the pure-system calculation (solid line) and consistent with the random-field calculation (dotted line), further supporting our proposal. The dotted line was calculated for a mean tilt angle of 1.2°. The dashed and dash-dotted lines, calculated for 0.6° and 1.7°, define the range of mean tilt angles that are consistent with the experimental data. We therefore conclude that MFT with randomness included accounts also for the field dependence of χ^{-1}.

It is important to note that in the experimentally accessible temperature range the results are insensitive to the details of the distribution, depending only on the mean square tilt angle. This is demonstrated by the dashed and dotted lines in Fig. 4.1. These show calculations of $\chi^{-1}(T)$ for 4 T and 5 T obtained using a different distribution of the random field with the same mean square tilt angle of 1.2° as above, but with 25% of the sites not tilted, and correspondingly larger tilts on the remaining sites. The dashed and dotted lines overlap in most of the temperature range. However, as is clear from the figure, the behavior of $\chi^{-1}(T)$ at lower temperatures does depend on the detailed distribution of tilts; χ^{-1} approaches zero (i.e. χ diverges) when the distribution includes spins that are not tilted. This conclusion can be experimentally tested, as the isomer distribution may be changed within this model by rotating the applied field in the plane perpendicular to the mean quantization axis [21, 73].

The effect of transverse field can be understood as follows. With or without randomness, a transverse field leads to a canting of the spins away from the z-axis, as illustrated in Fig. 4.2, and to enhanced quantum fluctuations of the spin. Since the intermolecular dipole interaction is associated with the z-component of spin, the dipole interaction strength is reduced in a transverse field. However, a transverse field much smaller than the anisotropy field $H_A \approx 10$ T produces very little spin canting ($\tan\theta_c = H_\perp/H_A$) and a negligible change in the interaction strength. Hence, for fields below about 3 T the susceptibility and the ordering temperature are virtually unchanged in the system without randomness. The FM order is very strongly suppressed only when the quantum fluctuations become important (when the tunnel splitting, Δ, of the lowest spin states is comparable to the intermolecular dipole interactions, which occurs at ~ 7 T for Mn_{12}-ac [19, 21]). However, in the presence of the tilt disorder described above, for transverse fields that establish longitudinal field components along the easy axis of tilted molecule comparable in magnitude to the intermolecular dipole field (approximately 50 mT [74], corresponding to 3 T for a tilt angle of 1°),

the tilted spins can no longer participate in the FM order and there is an effective dilution of the spins which causes a rapid reduction of the susceptibility and of the ordering temperature [21].

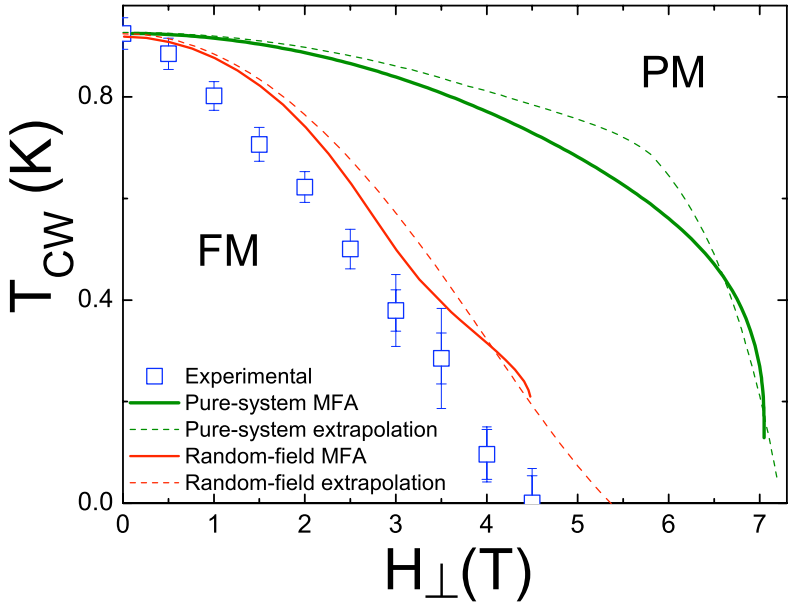

Figure 4.3: The Curie-Weiss and the ferromagnetic transition temperatures as a function of transverse field. The intercepts T_{CW} (squares) are obtained from the straight-line portion of the data curves in Figure 4.1. The dotted and dash-dotted lines are mean-field T_{CW} results for the pure and random case, respectively. The light and heavy solid lines are mean-field transition temperatures, T_C, calculated for the pure and random case, respectively. In the random case at higher field, the detailed structure depends on the specific details of the distribution of random fields. Here we plot T_C using the distribution obtained by Park [31] where 20% of the molecules are nominally in untilted sites and the parameters ($\theta = 1.2°$ and $\phi = 0$) are the same as those used to fit the data in Figure 4.1. For this assumed distribution and these parameters, T_C drops discontinuously to zero at 4.5 T.

Figure 4.3 shows approximate values of the intercept T_{CW} (squares) obtained from fitting the high-temperature region of the experimental curves shown in Figure 4.1 to the Curie-Weiss law. The fit does not include data for which $\chi^{-1} > 0.2$, as the measured susceptibilty exhibits a systematic background that reaches above 10% at values of $\chi = 0.5$. Data at high transverse field and low temperatures were also ignored (the upturns in Fig. 4.1); in this region the tunnel splitting becomes larger than kT

and, consequently, the susceptibility reflects the quantum state rather than being determined by the temperature. At small values of the transverse field the intercepts T_{CW} derived from extrapolation of the high temperature data provides a reasonably reliable estimate for the mean field transition temperature, but the extrapolations are less reliable as the transverse field is increased. Yet, the conclusion from Fig. 4.3 is clear: the application of transverse field leads to a strong, approximately linear reduction in T_{CW}. To estimate the reliability of the extrapolation and the significance of the strong reduction in T_{CW} we applied the same extrapolation procedure to the theoretical χ^{-1} curves for the "pure" and random case (solid and dashed lines in Fig. 4.1, respectively); the calculated intercepts are shown in Fig. 4.3 by the dotted and dash-dotted lines, respectively. We also used the theoretical model to calculate the mean-field paramagnetic-ferromagnetic transition temperature, T_C, i. e. the temperature where χ diverges ($\chi^{-1} = 0$). The calculated values of T_C for the pure and random cases are denoted in Fig. 4.3 by the solid dotted and dash-dotted lines, respectively. At low transverse fields (below 3 T), the calculated T_{CW} and the calculated ferromagnetic transition temperature T_C differ by less than 5%.

4.3 Conclusions

Based on measurements of magnetic susceptibility and magnetization, we find that the prototypical single molecule magnet Mn_{12}-ac is a new archetype of random-field Ising ferromagnetism in transverse field. In this system, although the intrinsic randomness in the interaction is small, it is sufficient for an externally applied transverse magnetic field to generate a significant random field in the longitudinal direction. In addition to canting the spins, the transverse field reduces T_{CW} in two ways: (1) it introduces channels for quantum relaxation for each of the molecules, thereby inducing spin disorder, and (2) it induces fluctuations in the longitudinal field that are comparable with the intrinsic dipolar interactions themselves, thereby further depressing the

ordering temperature. These factors give rise to a dependence of T_{CW} on $H_{\perp}$ that is inconsistent with that expected from mean field theory for a "pure" well-ordered system. We conclude that the rapid decrease of T_{CW} with increasing transverse field, as well as our ability to fit the susceptibility with a model that includes randomness, are strong evidence that Mn_{12}-ac is a particularly clean realization of random field Ising ferromagnetism in a new class of materials.

Chapter 5

Procedure for converting local Hall bar measurements to susceptibility in the presence of transverse field.

As mentioned in the previous Chapters, the inferred transition temperature T_{CW}'s for the two Mn_{12}-ac samples are different when obtained by the Hall sensor measurements. On the other hand, these two samples showed almost identical T_{CW} values when measured by the MPMS, as shown in Fig. 5.1. This is due to the Hall bar picking up the demagnetizing field differently in the different placements relative to the sample.

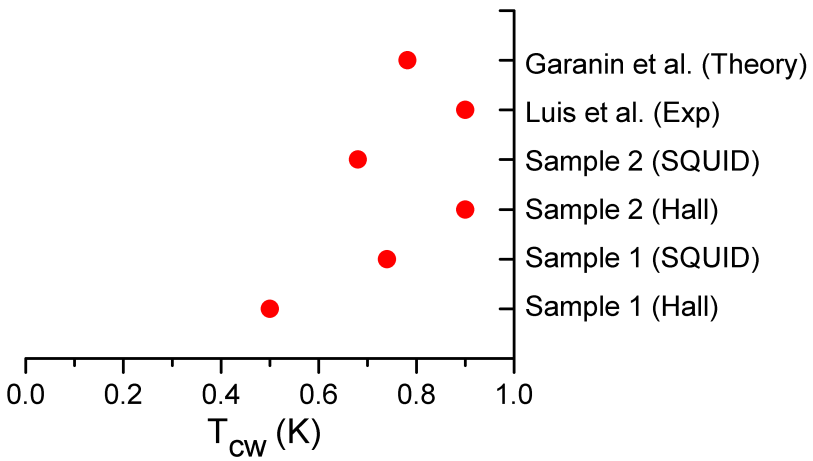

Figure 5.1: A comparison of T_{CW} measured by different methods and from different samples and theory prediction

The study in Ref. [62] of the dependence of T_{CW} on sample aspect ratio enables us

to correct the demagnetizing field using the MPMS measurement data. The procedure provides a method to determine the intrinsic susceptibility of the sample at zero $H_\perp$. However, we are interested in the effect of transverse magnetic field on the sample, but applying an $H_\perp$ in the MPMS is not a trivial task.

With the resources at hand, we chose to use Hall magnetometery in a 3-axis vector magnet for this study. Because the Hall sensor is only sensitive to the field perpendicular to its surface, if we use the configuration shown in Fig. 5.2, neither of the longitudinal or transverse external field will affect the reading.

By comparing the data of these two methods at zero $H_\perp$, we can calibrate the Hall magnetometery against the MPMS measurement. This will allow us to correct for the demagnetization effect in the transverse field data. The success of this method will open up a new field of studying the transverse field effect on the sample without the complication of demag effect.

To achieve this goal, we performed a series of magnetostatic calculations to unveil the relationship between χ_{Hall} and χ_{MPMS}:

MPMS measures the magnetic response using a SQUID. Its readout is the total magnetic moment of the specimen, from which we can get the magnetization $< M >$ by dividing the sample volume. $\chi_{MPMS} =< M > /H_\parallel$, where $H_\parallel$ is the applied field along the sample c-axis direction.

The Hall sensor output voltage V_{Hall} measures the stray field of a magnetized specimen, which is related to the sample magnetization $\mathbf{M}(x, y, z)$. Then an apparent susceptibility can be defined as $\chi_{Hall} = V_{Hall}/H_\parallel$.

We approximate the real experimental setup with the following ideal model:

1. Because the active Hall area is much smaller than the sample size, we assume B_x is approximately uniform within the Hall sensor area.

2. $\mathbf{J}_{free} = 0$, so

$$\nabla \times \mathbf{H} = 0 \;\Rightarrow\; \mathbf{H} \equiv -\nabla \Phi_M \tag{5.1}$$

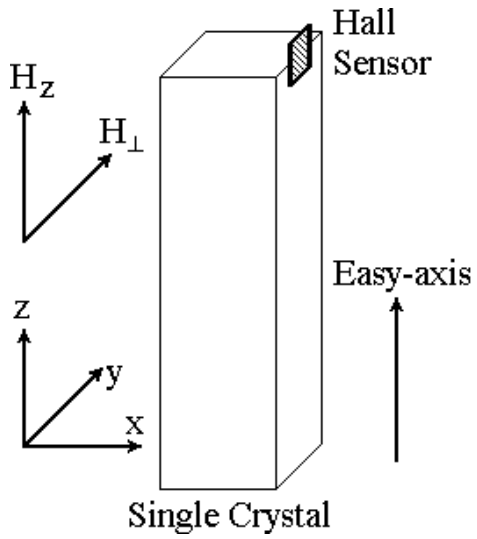

Figure 5.2: A rectangular prism sample has boundary $-x_0 < x < x_0$, $-y_0 < y < y_0$, $-z_0 < z < z_0$. The Hall sensor is located on surface $x = x_0$, centered at (x_0, y_1, z_1), expanded in the area $y_1 - a < y < y_1 + a$, $z_1 - b < z < z_1 + b$.

where Φ_M is the magnetic potential function.

3. $\mathbf{M} = 0$ outside, and $\mathbf{M} \neq 0$ inside.

$$\mathbf{B} = \mu_0 \cdot \mathbf{H} \text{ outside;}$$

$$\mathbf{B} = \mu_0 \cdot (\mathbf{H} + \mathbf{M}) \text{ inside.}$$

and

$$\nabla \cdot \mathbf{B} = 0$$

$$\therefore$$

$$\nabla \cdot \mathbf{H} = 0 \text{ outside;}$$

$$\nabla \cdot \mathbf{H} = -\nabla \cdot \mathbf{M} \text{ inside;}$$

$$\therefore$$

$$\nabla^2 \Phi_M = 0 \text{ outside;}$$

$$\nabla^2 \Phi_M = \nabla \cdot \mathbf{M} \text{ inside;}$$

The solution to the above equation about Φ_M is: [75]

$$\Phi_M(\mathbf{r}) = -\frac{1}{4\pi}\int_V \frac{\nabla' \cdot \mathbf{M}(\mathbf{r}')}{|\mathbf{r}-\mathbf{r}'|}d^3r' + \frac{1}{4\pi}\oint_A \frac{\mathbf{n}' \cdot \mathbf{M}(\mathbf{r}')}{|\mathbf{r}-\mathbf{r}'|}d^2r' \tag{5.2}$$

In order to solve this equation, we need an addition relation between M and H, which is discussed below.

5.1 Uniform magnetization

In this section, we will show that the assumption of uniform magnetization, which is commonly made in magnetic measurements, is not suitable here.

$\mathbf{M}$ is uniform means $\mathbf{M} = M_y\hat{y} + M_z\hat{z}$ inside the sample (we have applied field in both y and z direction). We will have $\nabla' \cdot \mathbf{M}(\mathbf{r}') = 0$, so only the second term is left:

$$\begin{aligned}\Phi_M(\mathbf{r}) = &\frac{1}{4\pi}\int_{-x_0}^{x_0}\int_{-z_0}^{z_0}\left(\frac{-M_y}{|(x,y,z)-(x',-y_0,z')|} + \frac{M_y}{|(x,y,z)-(x',y_0,z')|}\right)dx'dz' \\ &+ \frac{1}{4\pi}\int_{-x_0}^{x_0}\int_{-y_0}^{y_0}\left(\frac{-M_z}{|(x,y,z)-(x',y',-z_0)|} + \frac{M_z}{|(x,y,z)-(x',y',z_0)|}\right)dx'dy'\end{aligned}$$

$$\begin{aligned}B_x = H_x &= -\frac{\partial \Phi_M}{\partial x} \\ &= \frac{1}{4\pi}\int_{-x_0}^{x_0}\int_{-z_0}^{z_0}\left(\frac{x-x'}{|(x,y,z)-(x',-y_0,z')|^3} - \frac{x-x'}{|(x,y,z)-(x',y_0,z')|^3}\right)dx'dz' \cdot M_y \\ &+ \frac{1}{4\pi}\int_{-x_0}^{x_0}\int_{-y_0}^{y_0}\left(\frac{x-x'}{|(x,y,z)-(x',y',-z_0)|^3} - \frac{x-x'}{|(x,y,z)-(x',y',z_0)|^3}\right)dx'dy' \cdot M_z \\ &= G_1(\mathbf{r}) \cdot M_y(H_y) + G_2(\mathbf{r}) \cdot M_z(H_z)\end{aligned}$$

where $G_1(\mathbf{r})$ and $G_2(\mathbf{r})$ are geometric factors depending only on the location of the sensor. From this, we can deduce a commonly used approximation in Hall sensor measurements: the stray field B_x is a linear function of M_z.

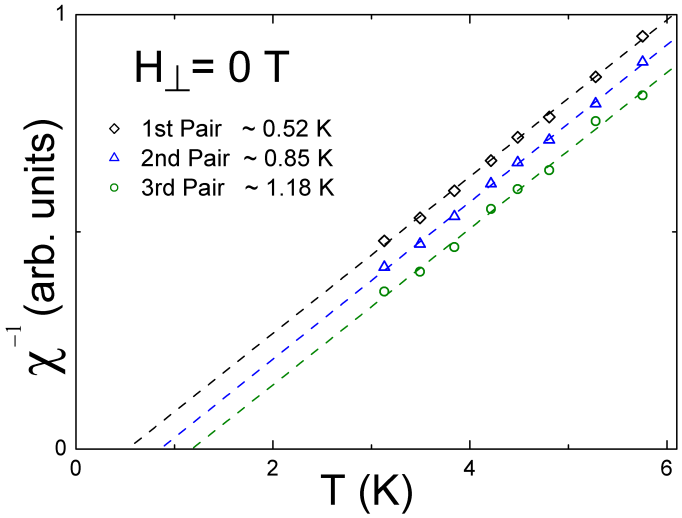

Figure 5.3: Apparent susceptibility versus temperature for sample C at zero transverse field. The values are normalized by each location's signal strength.

If the Hall sensor is placed in the center of the sample along the y-direction($y = 0$), the M_y term will vanish after averaging over the Hall area:

$$\begin{aligned} G_1(\mathbf{r}) &= \frac{1}{4\pi}\int_{-x_0}^{x_0}\int_{-z_0}^{z_0}\left(\frac{x-x'}{|(x,0,z)-(x',-y_0,z')|^3}-\frac{x-x'}{|(x,0,z)-(x',y_0,z')|^3}\right)dx'dz' \\ &= \frac{1}{4\pi}\int_{-x_0}^{x_0}\int_{-z_0}^{z_0}\left(\frac{x-x'}{((x-x')^2+y_0^2+(z-z')^2)^{3/2}}-\frac{x-x'}{((x-x')^2+y_0^2+(z-z')^2)^{3/2}}\right)dx'dz' \\ &= 0 \end{aligned}$$

thus $B_x \propto M_z$.

$\chi_z = \frac{\partial M_z}{\partial H_z}|_{H_z=0} = \frac{\partial(B_x - G_1 \cdot M_y)/G_2}{\partial H_z} = \frac{1}{G_2}\frac{\partial B_x}{\partial H_z}$. So the χ_z is only related to M_z whether or not the Hall sensor is placed at $y = 0$.

If this is true, when we measured the χ_z at different z positions of the sample, we should get results that can be normalized by only multiplicate factors, i.e., they should all intercept at the same point on the temperature axis.

First of all, this does not agree with the experiment observation, which is shown in Fig. 5.3, where in addition to normalization which is simply a calibration of the sensor signal strength, it is still necessary to shift the curves along the T axis to achieve the coincidence.

Secondly, as you will see in the next section, uniform magnetization is theoretically inconsistent with uniform susceptibility, which is a reasonable physical assumption to make.

Third, from magnetostatics we know that the magnetization of a non-ellipsoidal sample is non-uniform, and depends on both χ and sample shape [60, 61].

5.2 Uniform susceptibility

At the microscopic level, the susceptibility is $\chi = \frac{<S>}{H_{total}}$. In a simple picture, each Mn_{12} molecule in a SMM is identical, so that its response to the local field H_{total} should be the same. Thus, it is reasonable to assume that the χ for each molecule is the same. Then we can make an assumption of the relationship between M and H in order to solve Eq. 5.2 : a linear response with uniform susceptibility, i.e.:

$$\mathbf{M}(\mathbf{r}) = \chi \mathbf{H}(\mathbf{r}) \text{ inside} \tag{5.3}$$

From this equation and $\mathbf{B} = \mu_0(\mathbf{M} + \mathbf{H})$, we see that $\nabla \cdot \mathbf{B}(\mathbf{r}) = 0$ implies $\nabla \cdot \mathbf{M}(\mathbf{r}) = 0$ except at the edge of the sample.

Note that the reasoning for setting $\nabla \cdot \mathbf{M}(\mathbf{r}) = 0$ here is different from the case of uniform magnetization. Here, the magnetization varies in space, but the divergence of $\mathbf{M}$ is zero, meaning that there is no net magnetic pole / free current inside the sample, i.e., $\nabla \times \vec{H} = 0 \Rightarrow \vec{H} = -\nabla\phi$. All the magnetic field is induced by the surface magnetic poles $\sigma \equiv \mathbf{n}' \cdot \mathbf{M} = \mathbf{n}' \cdot \chi \mathbf{H}|_{\text{boundary}}$. Eq. 5.2 becomes:

$$\Phi_M(\mathbf{r}) = \frac{1}{4\pi} \oint_A \frac{\sigma(\mathbf{r}')}{|\mathbf{r} - \mathbf{r}'|} d^2 r'$$

$$\mathbf{H}_a + \mathbf{H}_{induced}(\mathbf{r}) = \mathbf{H}(\mathbf{r}) = \nabla \Phi_M(\mathbf{r}) = \frac{1}{4\pi} \oint_A \frac{\sigma(\mathbf{r}')(\mathbf{r} - \mathbf{r}')}{|\mathbf{r} - \mathbf{r}'|^3} d^2 r'$$

This is a integral equation for the applied field $\mathbf{H}_a$ and induced field for σ.

Then we use finite element analysis to solve this problem numerically, i.e., divide the surface into small pieces, such that the magnetization within each piece can be

regarded as uniform. To simplify the calculation, we approximate the crystal shape by a square bar with $l_a = l_b \cdot l_c$ measured as described in section 3.5.2. Then we apply the method of Pardo *et al.* [63, 64], which is briefly summarized below, for the surface division: The division elements are rectangular in shape, with size smaller on the edges and corners where the magnetization varies strongly in space, and bigger in the middle of the sample where the magnetization changes slowly.

This leads to

$$\mathbf{H}(\mathbf{r}) = \frac{1}{4\pi} \sum_{i=0}^{N} \frac{\sigma_i A_i (\mathbf{r} - \mathbf{r_i}')}{|\mathbf{r} - \mathbf{r_i}'|^3} \tag{5.4}$$

where A_i is the area of ith piece, $\mathbf{r_i}'$ is the coordinate of the center of ith piece. We will be able to calculate the magnetic field distribution once we know σ_i, which can be obtained by solving Eq. 5.5:

$$\begin{aligned} \mathbf{M} &= \chi(\mathbf{H}_a + \mathbf{H}_d) \Rightarrow \\ \frac{\mathbf{M}}{\chi} - \mathbf{H}_d &= \mathbf{H}_a \Rightarrow \\ \frac{\sigma_i}{\chi} - \sum_{j=0}^{N} \mathbf{e}_n^i \mathbf{D}_{ij} \sigma_j &= \mathbf{e}_n^i \cdot \mathbf{H}_a \end{aligned} \tag{5.5}$$

where $\mathbf{e}_n^i$ is the outward unit vector normal to the ith element, and $\mathbf{D}_{ij}\sigma_j$ is the induced demagnetizing field generated by the jth element applied on the ith element, with $\mathbf{D}_{ij} = \frac{A_j(r_i - r_j)}{|r_i - r_j|^3}$, as derived in Appendix 8.1. (The Mn_{12} molecule is anisotropic. The details of procedures for accounting the effect of the anisotropy in the calculation are presented in Appendix 8.2.)

From Eq. 5.5, we can immediately know the following: when χ is small, σ is proportional to $\mathbf{e}_n^i \cdot \mathbf{H}_a$, i.e., there are only surface charge in the top and bottom surface of the sample in Fig. 5.2; when χ is big, the induced term become important and the behavior become non-linear. We will discuss this point again in Sec. 5.4.

The combination of Eq. 5.4 and 5.5 gives us a relationship between the intrinsic χ and the magnetic field $\mathbf{H}$ generated by the crystal at any specific spatial point. Fig.

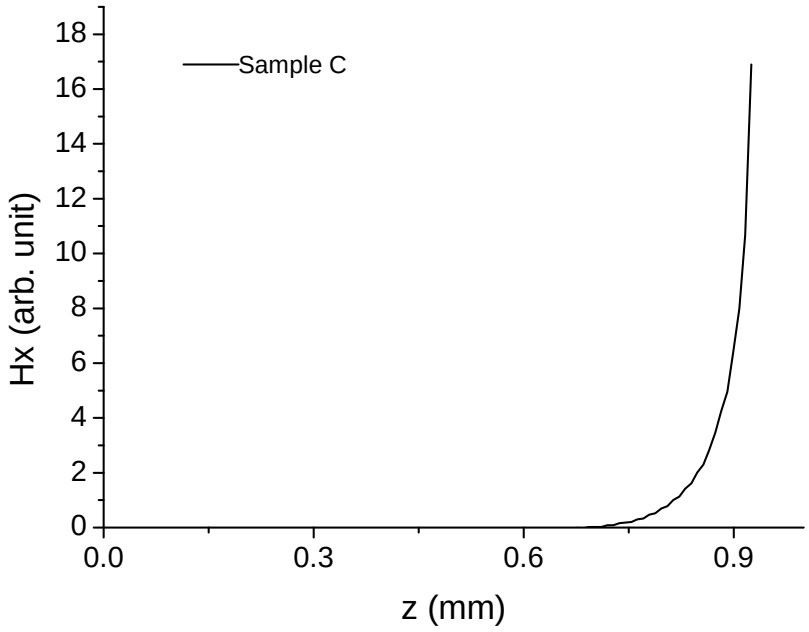

Figure 5.4: plot of calculated result of $\mathbf{H}_x|_{y=0}(z)$.

5.5 is the plot of the induced magnetic field in three directions on the surface of the crystal. As expected, the field in the x direction is bigger near the end of the crystal. When we integrate the x component of the field over the area where the Hall sensor is positioned, we can get the expected Hall sensor signal:

$$V_{Hall-cal}(\mathbf{r}) = A \cdot < H_x(\mathbf{r}) > \tag{5.6}$$

where the coefficient $A = R_H \cdot I/d$ is obtained in the experiment by measuring the Hall sensor response as a function of magnetic field applied perpendicular to the surface.

This process can be summarized by expressing the Hall sensor signal as a function ζ of the intrinsic susceptibility:

$$V_{Hall-cal}(T) = \zeta_{\{\mathbf{r},c/a,H_\perp,A\}}(\chi_{intrinsic}(T)) \tag{5.7}$$

where ζ is a function of the parameters $\mathbf{r}$ (the location of Hall sensor), c/a (aspect ratio of the sample), $H_\perp$ (applied transverse field) and A (Hall coefficient of the sensor).

Now we can obtain the apparent susceptibility $\chi_{Hall-cal} = V_{Hall-cal}/H_a$.

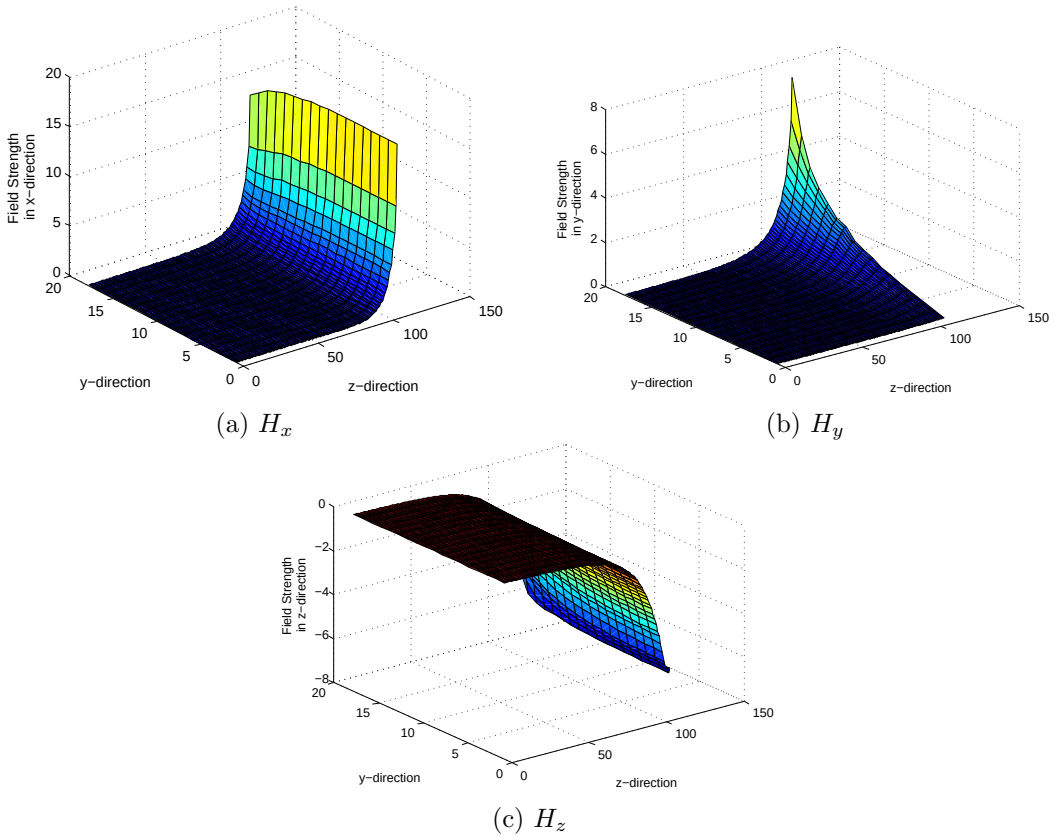

(a) H_x (b) H_y

(c) H_z

Figure 5.5: The distribution of the magnetic field on the y-z surface of the crystal (Sample C). The coordinate is defined in Fig. 5.2 with $y_0 = 1.85$ mm and $z_0 = 0.3$ mm. But the unit here is arbitrary unit chosen to accelerate the calculation.

5.3 Demagnetizing Correction

As shown in the inset of Fig. 3.6, over the range of our measurement, the system indeed has a linear response relationship between **M** and **H**. Thus we can calculate the expected Hall sensor signal (shown as round dots in Fig. 5.6) for a particular set of $\{\mathbf{r}, c/a, A\}$ at $H_\perp = 0$ using the ζ, given that the $\chi_{intrinsic}$ (shown as the square in Fig. 5.6) can be obtained from the MPMS measurements as described in Ref. [62].

However, if we plot the measured Hall sensor signal $\chi^{-1}_{Hall-meas}$ vs T (shown as the triangle in Fig. 5.6)., we find that they do not coincide with the expected value. Again additional shift in the temperature axis and a multiplication are required to collapse the lines together. The multiplication is not surprising. It is essentially a

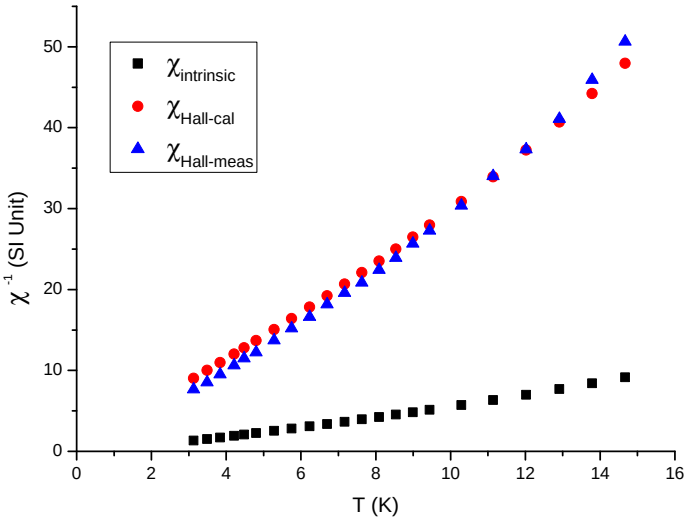

Figure 5.6: Temperature dependence of the intrinsic and apparent (both calculated and measured) inverse susceptibility of Mn_{12}-ac for zero transverse field obtained from global SQUID based measurements (Ref. [62]) and local Hall-sensor measurements (sample C, sensor P1), respectively.

calibration of the signal amplitude.

Both $\chi^{-1}_{Hall-meas}$ and $\chi^{-1}_{Hall-cal}$ are linear between 3K and 6K, which can be denoted as $\chi^{-1}_{Hall-cal} = a_1 \cdot (T - T_1)$ and $\chi^{-1}_{Hall-meas} = a_2 \cdot (T - T_2)$. We can eliminate the T in the equations to get $\chi^{-1}_{Hall-cal} = a_1 \cdot (\chi^{-1}_{Hall-meas}/a_2 + T_2 - T_1)$.

The difference between the $\chi_{Hall-cal}$ and $\chi_{Hall-meas}$ originates from several factors, including the uncertainty in the measured coefficient A, the uncertainty of Hall-sensor active area, deviations from the assumed sample shape from rectangular prism and etc.

None of these factors are affected by a transverse magnetic field, i.e., the fitting constant a_1, T_1 and a_2, T_2 are determined by factors other than $H_\perp$. In order to interpret our results in $H_\perp$, we now apply the same horizontal shift and multiplication to the $\chi_{Hall-meas}(T)$ to get the $\chi_{Hall-cal}$ in $H_\perp \neq 0$ cases. Then we use relationship Eq. 5.7 to deduce the $\chi_{intrinsic}(T)$ from the inferred $\chi_{Hall-cal}$. This process can be abstracted as following:

$$\chi_{Hall-meas}(T) \xrightarrow{\chi^{-1}_{Hall-cal}=a_1\cdot(\chi^{-1}_{Hall-meas}/a2+T_2-T_1)} \chi_{Hall-cal}(T) \xrightarrow{Eq.5.7} \chi_{intrinsic}(T) \quad (5.8)$$

In Fig. 5.7 we compare the resulting $\chi_{intrinsic}(T)$ with a $\chi_{MFA}(T)$ calculated using the RFIFM model described in Chapter 4 and Ref. [21,67]. The MFA calculation is a totally different approach, the agreement between the two methods provides validation of the assumptions we made in this demagnetization correction.

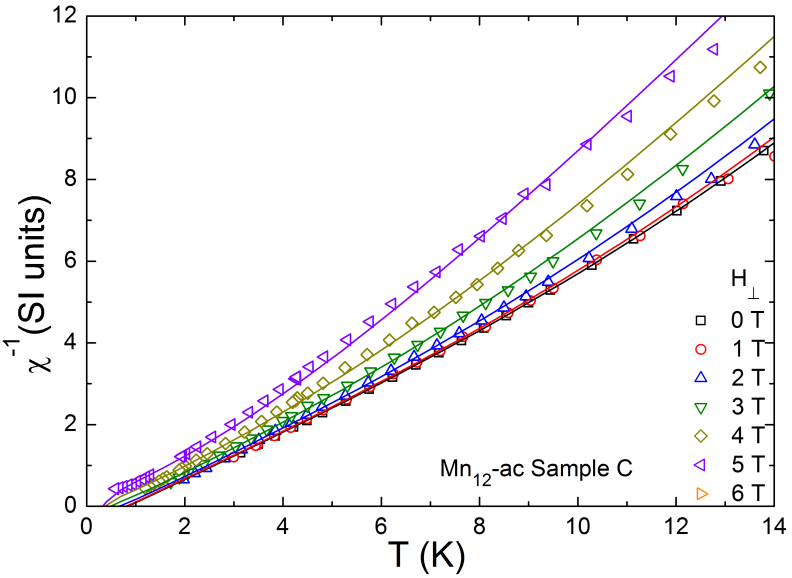

Figure 5.7: Susceptibility versus temperature at different transverse magnetic field for Mn_{12}-ac sample C. The symbols denotes the $\chi_{intrinsic}$. The lines are χ_{MFA}.

5.4 Discussion

1) According to the calculation, when $\chi_{intrinsic}$ is small ($\chi < 100$ in SI unit), the relationship between the spatial distribution of the magnetization and $\chi_{intrinsic}$ is close to linear, meaning that when the $\chi_{intrinsic}$ changes, the magnitude of H_x at different positions changes with fixed ratio. But when $\chi_{intrinsic}$ becomes big, the relationship becomes non-linear. As shown in Fig. 5.8, when $\chi_{intrinsic}$ goes towards infinity, i.e., when $\chi^{-1}_{intrinsic}$ goes towards its intercept point, the behavior becomes strongly non-linear and the $\chi_{Hall-cal}$ lines bend towards the same intercept. This explains why a linear extrapolation from high T, far from the intercept, gives intercepts differently from the MPMS result.

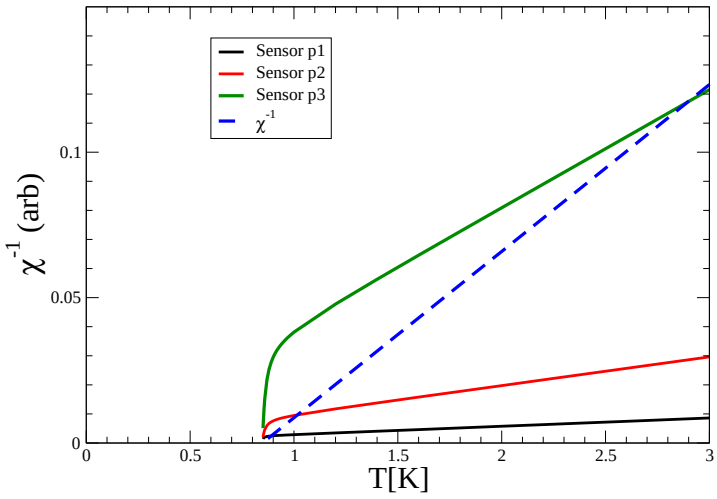

Figure 5.8: Susceptibility versus temperature for Mn_{12}-ac sample C. The solid lines are apparent susceptibility measured from three different locations. The broken line is the intrinsic susceptibility.

This agrees with the observation of Eq. 5.5 in Sec. 5.2.

2) As a sanity check, I performed the following calculation: First, obtain the $\chi_{intrinsic}(T)$ using Eq. 5.8 from $\chi_{Hall-meas}(T)$ of sensor 1. Then simulate the $\chi_{Hall}(T)$ at other sensor locations using Eq. 5.7 and the $\chi_{intrinsic}(T)$ gotten from sensor 1. Fig. 5.9 shows that the simulated result agrees with the measured data.

3) For both Mn_{12}-ac and Mn_{12}-ac-MeOH, the $\chi_{intrinsic}$ is on the order of magnitude of 0.5 in SI unit between 3K and 6K. The relationship between $\chi_{Hall-cal}$ and $\chi_{intrinsic}$ described by Eq. 5.7 becomes linear: $\chi^{-1}_{intrinsic} = a_3 \cdot \chi^{-1}_{Hall-cal} + b_3$. As a result, the whole demagnetization correction process is also reduced to a simplified linear form: $\chi^{-1}_{intrinsic} = a_3 \cdot (a_1 \cdot (\chi^{-1}_{Hall-meas}/a_2 + T_2 - T_1)) + b_3$.

This simplified version is used in the data analysis of Chapter 6 and Ref. [67].

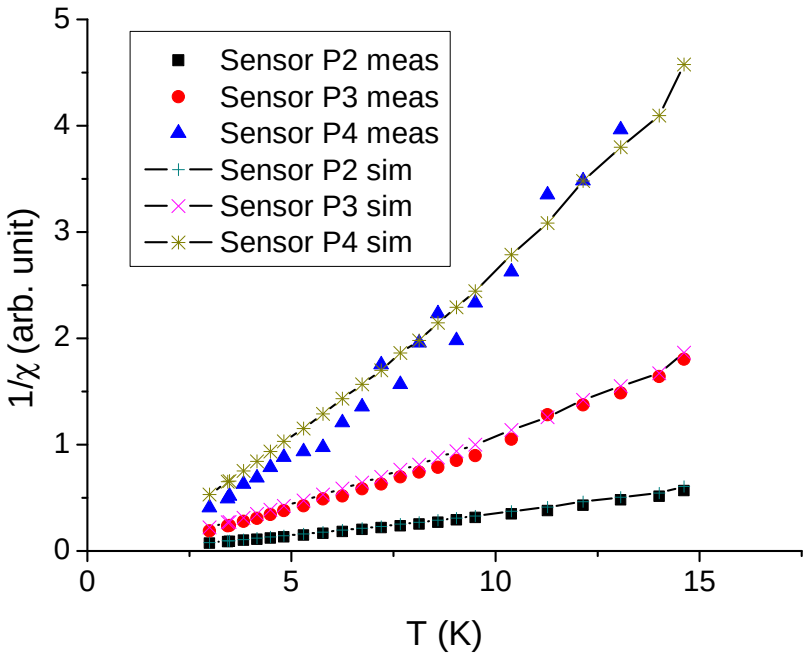

Figure 5.9: Simulation result and measurement data of Sample C at $H_\perp = 1$ T.

5.5 Summary

We demonstrated a method to interpret the Hall sensor local measurement in transverse magnetic field by calibrating the demagnetization effect in zero transverse field. In the following chapter, we will apply this method in the study of Mn_{12}-ac-MeOH.

Chapter 6

Comparison experiment: transverse field Ising ferromagnetism in Mn_{12}-ac-MeOH

Dipolar interactions can lead to long range magnetic order. However, the application of a magnetic field in a direction transverse to the Ising axis induces quantum spin fluctuations that compete with the long-range order by mixing the eigenstates of S_z [76]. This interplay between the long range order and spin fluctuations is described by the Transverse-Field Ising Hamiltonian:

$$\mathcal{H} = \frac{1}{2}\sum_{i \neq j} J_{ij} S_i^z S_j^z + \Delta \sum_i S_i^x \tag{6.1}$$

Here, S_i is a two level Ising spin on lattice site i, J_{ij} are the dipolar couplings and Δ is the tunnel splitting that depends on the applied transverse field [21]. This Hamiltonian applies at energies and temperatures such that excitation to higher energy states of the molecular complex can be neglected; for the systems of interest in this thesis Eq. 6.1 applies below a transverse-field-dependent temperature $\lesssim 6$ K.

Mn_{12}-ac is not simply a representation of the transverse-field Ising model, as detailed in Ch. 4, because a distribution in the arrangements of the solvent molecules results in a distribution of discrete tilts of the molecular magnetic easy axis from the global (average) easy axis of a crystal, thereby locally breaking the global tetragonal symmetry of the crystal [27–30]. Although the small molecular easy-axis tilts ($\approx \pm 1^\circ$)

induce only minor perturbations in the dipolar interaction, an external transverse magnetic field has projections along (the randomly distributed) easy axes that become comparable in magnitude to the dipolar field itself for transverse field magnitudes of order 4 T [20, 21]. It was shown in Ch. 4 and Ref. [20, 21] that one can account for the experimental data for Mn_{12}-ac by adding a site transverse field-dependent random-field term $\sum_i h_i S_i^z$ to Eq. 6.1 so that this prototypical molecular magnet is a realization of the Random-Field Ising Ferromagnet (RFIFM).

In this chapter, we report results of an investigation of Mn_{12}-ac-MeOH. The two systems differ only in the isomer disorder introduced by the solvent molecules in Mn_{12}-ac, so that a comparison of their magnetic response provides quantitative information about the effect of random fields. We find that the behavior of Mn_{12}-ac-MeOH is consistent with Eq. 6.1 without disorder effects at intermediate temperatures, where the new "pure" MeOH variant represents a model-system for the study of intrinsic transverse-field Ising magnetism. However, there are deviations from simple theoretical expectations for both Mn_{12} variants below about 2 K that are not currently understood and require further study.

6.1 Experiment

Measurements of the longitudinal magnetization and susceptibility were performed on three Mn_{12}-ac-MeOH single crystals of dimensions $\sim 0.2 \times 0.2 \times 0.95$ mm^3, $0.085 \times 0.085 \times 0.68$ mm^3, and $0.075 \times 0.075 \times 0.65$ mm^3 (samples D, E and F, respectively). The experimental setup and crystal handling have been described in Ch. 3.

The field dependence of the magnetization of Mn_{12}-ac-MeOH (Sample F) is shown in the main panel of Fig. 6.1 for temperatures below 1 K in the absence of transverse magnetic field. Characteristic of resonant tunneling in molecular magnets, the steps occur due to faster spin-reversal at specific (temperature-independent) magnetic fields corresponding to energy-level coincidences on opposite sides of the

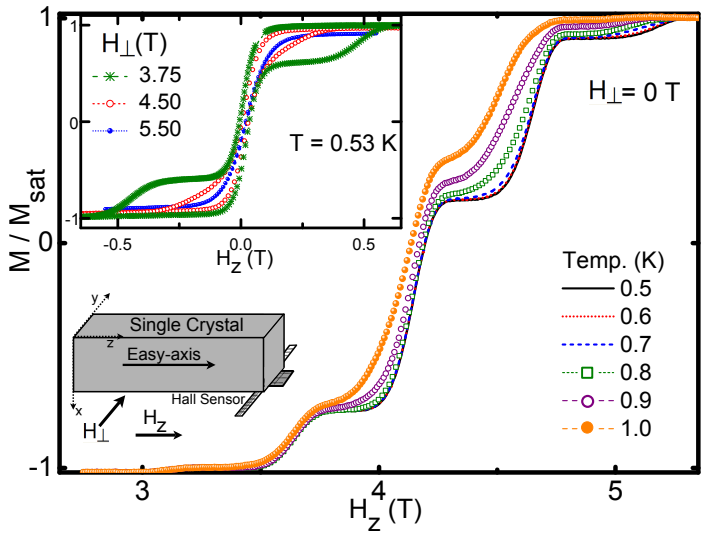

Figure 6.1: Normalized magnetization of Mn_{12}-ac-MeOH as a function of longitudinal magnetic field, H_z, in zero transverse field at several temperatures below 1 K. The sweep rate of H_z in the main panel and the top inset is 1.67 mT/s. Top Inset: Magnetization vs H_z at $T = 0.53$ K for different transverse fields, $H_\perp$. Bottom Inset: Schematic diagram of the sample, the Hall sensor and magnetic fields.

anisotropy barrier [4]. The resonant fields at which the steps occur in Mn_{12}-ac-MeOH are the same as in Mn_{12}-ac, indicating that the two systems have similar spin energy-level structures. The magnetization exhibits hysteresis due to slow relaxation below a blocking temperature, T_B, that depends on the rate at which the magnetic feld is swept. Equilibrium can be established as described in Sec. 3.4 by increasing the temperature and/or decreasing the sweep rate. It can also be promoted by applying a transverse magnetic field. The latter is demonstrated in the top inset of Fig. 6.1 which shows the low-field magnetization in transverse field at 0.53 K. While hysteresis is evident for $H_\perp = 3.75$ T, the system is in equilibrium at the higher field of $H_\perp = 5.5$ T; by mixing the eigenstates of S_z, the transverse field promotes quantum tunneling and accelerates relaxation toward equilibrium.

Under equilibrium conditions, the longitudinal magnetic susceptibility, $\chi \equiv \partial M_z/\partial H_z|_{H_z=0}$, can be deduced from the slope of M_z versus H_z at $H_z = 0$ as described in Ch.4 and Ref. [20]. Figures 6.2(a) and 6.2(c) show the inverse susceptibility of a Mn_{12}-ac-MeOH

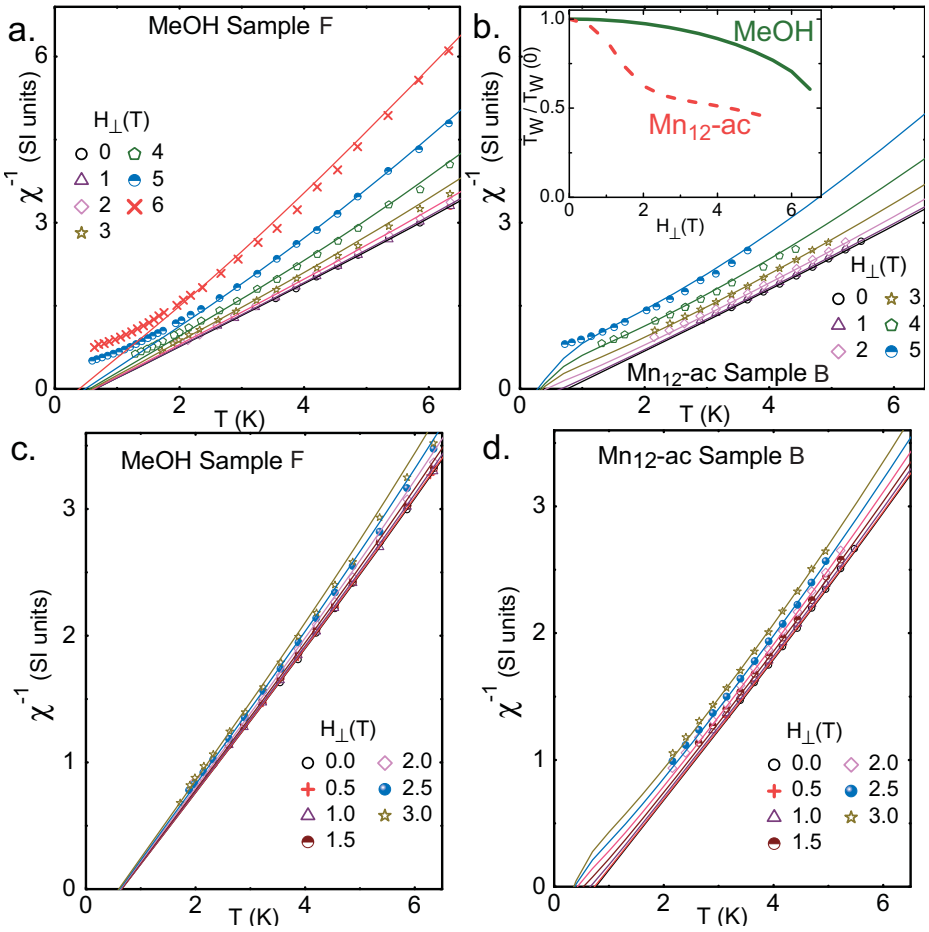

Figure 6.2: (a): Inverse susceptibility as a function of temperature for Mn_{12}-ac-MeOH (Sample F) in various transverse fields up to 6 T. (b): Inverse susceptibility as a function of temperature of Mn_{12}-ac (Sample B) for various transverse fields up to 5 T. (c) and (d) Inverse susceptibility in low transverse field up to 3 T for Mn_{12}-ac-MeOH and Mn_{12}-ac, respectively. The solid lines are theoretical curves based on Eq. 6.2. Inset to frame (b): The Weiss temperature $T_W(H_\perp)$, normalized to T_W in zero transverse field, for Mn_{12}-ac-MeOH (solid green) and for Mn_{12}-ac (dashed red) obtained from fits to the theory in the range $2-6$ K. The dashed lines are the theoretical curves based on Eq. 6.2 with $\theta = 1.8\,^\circ$.

(Sample F) crystal as a function of temperature for various fixed transverse magnetic fields between 0 and 6 T. The data were corrected for demagnetization effects, as described in the Ch. 5. The inverse susceptibility increases with transverse field (the susceptibility χ decreases) due to spin canting. An unexpected flattening of the curve occurs for temperatures below $\sim$ 2 K. For comparison, we show similar data obtained for a Mn_{12}-ac (Sample B) crystal in Figs. 6.2(b) and 6.2(d); the expected

overall decrease of the susceptibility with transverse field is also observed, as well as the anomalous deviations at low temperature. On the other hand, it is clear that the response to transverse field is distinctly different for the two systems: while the slopes of the χ^{-1} vs. T curves increase rapidly for Mn_{12}-ac-MeOH, the curves remain approximately parallel with little change of slope in the case of Mn_{12}-ac, with a concomitant rapid decrease of the apparent intercept and Weiss temperature, as reported earlier for this random system [20].

To further demonstrate the different response to the magnetic field, and guided by Eq. 6.2 below, we plot in Fig. 6.3 the normalized change $\Delta\chi^{-1}(H_\perp)$ of the inverse susceptibility at a particular temperature, as a function of $H_\perp^2$ for three Mn_{12}-ac-MeOH samples (green dots) and three Mn_{12}-ac (red squares) at T = 3.2 K. We note that the subtraction, $\Delta\chi^{-1}(H_\perp) = \chi^{-1}(H_\perp) - \chi^{-1}(0)$, eliminates the intermolecular interaction term (J), and the normalization removes the dependence on sample volume. Figure 6.3 clearly shows that the effect of the transverse field is much larger for Mn_{12}-ac.

To analyze the data quantitatively we turn to the theoretical expression presented in Ref. [21]:

$$\chi^{-1}(H_\perp, T) = C\left(\sec^2\theta(H_\perp)\frac{\Delta(H_\perp)}{\tanh\frac{\Delta(H_\perp)}{T}} - J\right). \tag{6.2}$$

Here J is the effective exchange interaction obtained from the appropriate spatial average over the dipole interaction, the angle θ characterizes the spin canting in an applied transverse field and Δ is the tunnel splitting; detailed expressions for the dependence of θ and Δ on $H_\perp$ are given in Ref. [21]. The bottom line is that the tunnel splitting becomes non-negligible only for $H_\perp > 6T$ while in the range $0 < H_\perp < 5T$, $\theta\ [rad] \approx 0.1 H_\perp\ [T]$.

Using Eq. 6.2, we plot in Fig. 6.3 the change $\Delta\chi^{-1}$ of the inverse susceptibility, normalized to the zero transverse field inverse susceptibility value,

$$\Delta\chi^{-1}(H_\perp) = \frac{\chi^{-1}(H_\perp) - \chi^{-1}(0)}{\chi^{-1}(0)}, \tag{6.3}$$

for the "pure" Transverse Field Ising Ferromagnet with no tilt angle (green solid line) and for the Random Field Ising Ferromagnet (RFIFM) with the mean square tilt angle of 1.8 ° (red dashed line) for the random-field distribution proposed by Park et. al [31]. The excellent agreement between calculation and data for the MeOH material at $H_\perp < 4T$ at 3.2 K is an indication that this system is a realization of the dipolar Ising model in a transverse field. A good fit is obtained for the Mn_{12}-ac crystal data with the RFIFM model using root mean square tilt angles of 1.8 °.

The different amount of disorder in the two systems demonstrated in Fig. 6.3 is also reflected in the temperature dependence of the susceptibility. The theoretical predictions for $\chi^{-1}(T)$ for a pure Mn_{12} system and for a system with an average tilt angle of 1.8 ° are shown by the solid lines in Fig. 6.2(a) and 6.2(b), respectively. The demagnetization correction is obtained by requiring that theory and experiment coincide at zero field. Within this assumption, the data between 2 and 6 K are consistent with theory for both samples, where a particularly good fit is obtained for fields below 3 T. However, while the theoretical lines intersect the temperature axis at $T_W(H_\perp)$ implying the approach to a ferromagnetic phase, the measured susceptibility deviates from this simple behavior, flattening as the temperature decreases toward the presumed transition. The behavior observed at these low temperatures is not understood, and may imply that a transition to a new phase is prohibited for reasons that are unclear. It is nevertheless interesting to examine the Weiss temperatures $T_W(H_\perp)$ predicted by the theory. This is shown in the inset to Fig. 6.2(b) for both samples, based on fits of the susceptibility measured between 2 and 6 K, where the "phase diagram" for the pure case is denoted by the green solid line

and the red dashed line denotes the theoretical prediction for the disordered case with average tilt angle of $\theta = 1.8\,^{\circ}$. For the theoretical calculation, the dipolar part of the interaction was obtained using the measured lattice parameters and crystal structure of Mn_{12}-ac-MeOH and the spin canting and tunnel splitting were obtained as described in Ref. [21]. A phase diagram similar to that observed for Mn_{12}-ac-MeOH was obtain by Burzuri *et al.* in Fe_8 [77].

The initial suppression of T_W for transverse fields $H_\perp < 5$ T (see inset to Fig. 6.2(b)) is expected due to spin canting, which reduces the net moment in the axial direction; the more rapid suppression at higher fields derives from the tunnellng term. A substantially more rapid suppression of T_W with $H_\perp$ is evident for Mn_{12}-ac. The results for Mn_{12}-ac are consistent with a modified theory that includes the effects of random fields arising from the tilt angles.

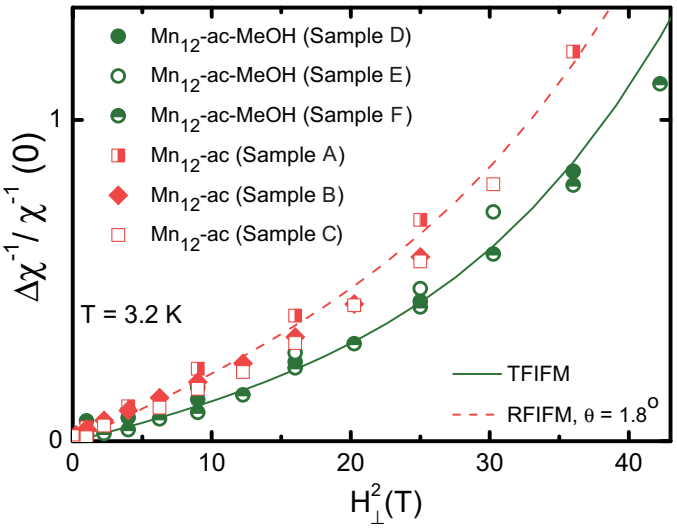

Figure 6.3: The change in inverse susceptibility, $\Delta\chi^{-1}$, normalized to the susceptibility at zero field versus $H_\perp^2$ for Mn_{12}-ac-MeOH (green dots, open circle Ref [20]) and Mn_{12}-ac (red squares, half filled and solid squares are Sample D and E in Ref [20]) at $T = 3.2$ K. The red dashed line is calculated using the random-field model of [20] (RFIFM) for the root mean square tilt angle of $1.8\,^{\circ}$. The solid green line shows the result for the case with no tilt angle (TFIFM).

In summary, these studies demonstrate that the magnetic susceptibility of Mn_{12}-ac-MeOH

follows the behavior expected for a transverse field Ising ferromagnet, in marked contrast with Mn_{12}-ac. The temperature dependence of the susceptibility and the dependence of the (extrapolated) Weiss temperature on applied transverse field are different for the two materials. More broadly, the availability of these two very similar SMMs with distinct types of magnetism provides unique opportunities for experimental studies of the effect of randomness on quantum phase transitions and magnetic relaxation. In particular, large transverse fields ($\sim$ 5 T) that enhance pure quantum tunnel relaxation (tunneling relaxation without the need for thermal activation) will enable equilibrium susceptibility studies down to very low temperature (mK). Such investigations may reveal interesting ground states (ferromagnetic, spin glass, or even antiferromagnetic) that may differ for the pure and random systems.

Chapter 7

Conclusions

This thesis reports our study of the dipolar interaction and dipolar long-range order in two single molecule magnets, Mn_{12}-ac and Mn_{12}-ac-MeOH. In both materials, the susceptibility is found to obey a Curie-Weiss law with a positive Weiss temperature, implying a transition to long-range order at low temperatures in agreement with earlier findings in Mn_{12}-ac. A magnetic field applied transverse to the easy-axis of the crystal reduces the Weiss temperature, suppressing the long-range ferromagnetic order. However, the temperature intercept is reduced far more rapidly in Mn_{12}-ac than Mn_{12}-ac-MeOH. We have attributed this to the presence of a random field in the former and its absence in the latter.

In the Mn_{12}-ac system, isomer disorder tilts the individual spins away from the global easy-axis, thereby creating a random field in the presence of a transverse field. In addition to the reduction of the Weiss temperature associated with tilt and thermal fluctuations, this random field further suppresses the long-range order. In our experiment, we observed that the dependence of T_{CW} on $H_{\perp}$ is much stronger than the mean-field expectation for a pure transverse field Ising ferromagnet model system.

To confirm the validity of our proposal that the rapid suppression in Mn_{12}-ac is indeed due to random fields associated with isomer disorder, we did a comparison experiment in Mn_{12}-ac-MeOH, which is known to be a much cleaner system without

isomer disorder. The result of the comparison experiment shows that the Mn_{12}-ac-MeOH is indeed consistent with that expected for a pure transverse field Ising ferromagnet. Given that the most important difference between the two systems is the isomer disorder, we conclude that the difference in their magnetic behaviors originates from the isomer disorder in a way described by the random field model theory.

This discovery provides a new prototype system to study the random field theory. Compared to the only other known random-field system, LiHoY, the Mn_{12}-ac has two clear advantages: first, hyperfine fields which complicated the analysis in LiHoY, are negligibly small in Mn_{12}-ac; second, the strength of the random field in Mn_{12}-ac system is controlled directly by the applied transverse field rather than by doping. These features make the Mn_{12}-ac a more favorable tool for studying random field effects. However, a disadvantage is that it is difficult to reach the ferromagnetic phase due to strong blocking. It is important to search for other molecular magnets in which these effects are more easily studied.

7.1 Future study

7.1.1 Thermal diffusivity of Mn_{12}-ac

Comparison of experimental results for magnetic avalanches obtained by Sean McHugh with the theory of magnetic deflagration of Garanin and Chudnovsky implies surprising (and perhaps unphysical) behavior of the temperature dependence of the thermal diffusivity κ of Mn_{12}-ac [78]. Sean Mchugh's attempts to measure the thermal diffusivity to resolve this issue were unsuccessful. I propose a method for performing these measurements.

The thermal diffusivity κ is related to the thermal conductivity, k, by the heat capacity C: $k = \kappa C$. As suggested by McHugh, one can measure the thermal conductivity k and then deduce κ using published values of the specific heat. Measuring k is less challenging because it can be done through a steady state measurement,

but it is still very difficult since the Mn_{12}-ac has a very high thermal resistance. The technical challenges lie in how to reduce the parallel thermal path and increase conductivity of the in-series thermal contacts. After some literature search [79–81], I propose the following setup to achieve these two goals:

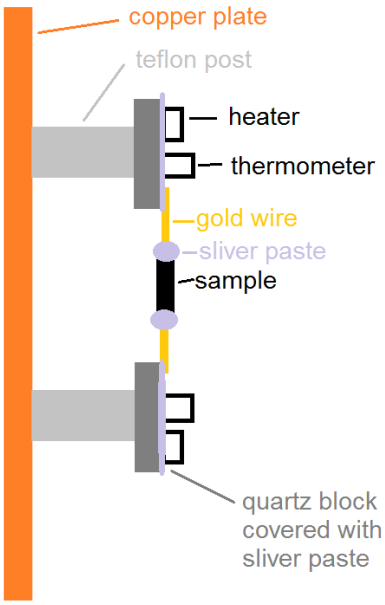

(a) schematic of experiment setup

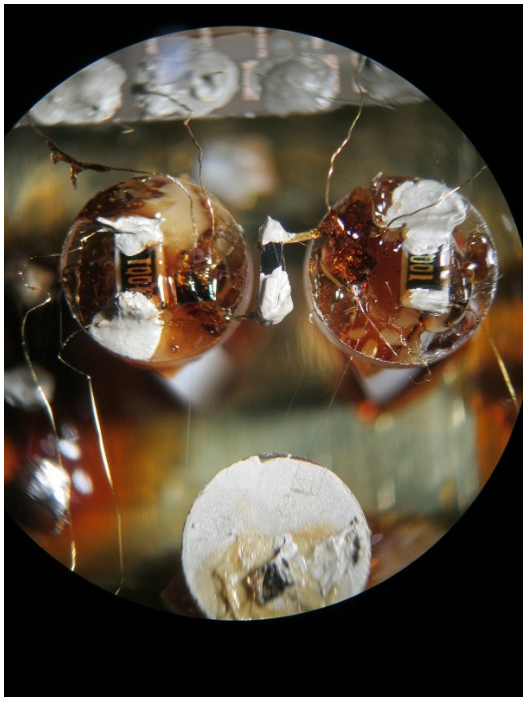

(b) photo of the real setup

Figure 7.1

As shown in Fig. 7.1a, a copper plate is used as the base for mechanical support and thermal anchor. Three teflon posts are glued on the plate with GE-vanish, and on top of each post is a quartz block. Because teflon has very low thermal conductivity at low temperature [82], it will minimize the thermal link between the quartz block and the copper base. In turn, the quartz block has a very high surface thermal conductivity, so when we glue the thermometer, heater and gold wire on the top of the same quartz block, they will be kept at the same temperature. Between the two quartz blocks, a Mn_{12}-ac single crystal is connected by gold wire as shown in Fig. 7.1b. The flexibility of gold wire ensures that the fragile Mn_{12}-ac single crystal won't

be stretched and break during the cool-down. The joint is made by silver paste to ensure good thermal contact. The third post is used as a reference for radiation heat transfer. There is a thermometer glued on its top surface.

In Sean's preliminary study, the thermal conductance was estimated to be ~ 10.5 W/K [78]. The thermal conductance of a normal cryogenic measurement apparatus is about the same order of magnitude, which presents a parallel thermal path that will short out the sample. To reduce this thermal path, we use a thermal isolation plate as shown in Fig. 7.2a. It is a glass slide coated with 5 nm thick gold film bars. The electrical connections are all first anchored on the copper base, then connected to one side of the gold film bar, then the other side of the gold film bar is connected to the thermometers and heaters on the quartz block. The 5 nm gold film provides enough electrical conductance (~ 1 kΩ), while the thermal conductance is expected to be very low.

(a) photo of the thermal isolation plate

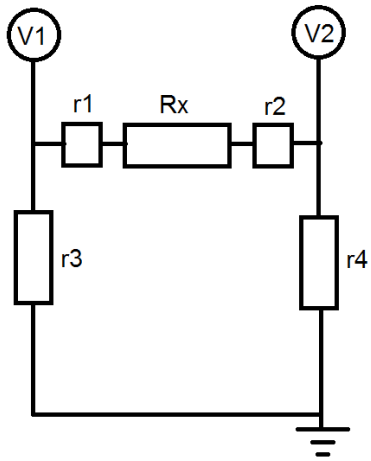

(b) the equivalent electric circuit of the measurement setup

Figure 7.2

Fig. 7.2b shows the equivalent electrical circuit of this thermal measurement setup. V_1 and V_2 are the source, in this case the two heaters. The potential (temperature) of the source is measured by the two thermometers on the same quartz block with the heater. The ground is the copper plate, its potential (temperature) is controlled by the cryostat and measured by the thermometer glued on it. R_x is the thermal resistance (conductance) of the Mn_{12}-ac crystal. r_1 and r_2 are the in-series resistances between the source and Rx; in our case, they include the thermal contact resistance between the gold wire and the crystal and between the gold wire and the quartz block, and the thermal resistance of the gold wire itself. Compared to the high resistance (low conductance) of the Mn_{12}-ac crystal, r_1 and r_2 can be safely ignored. r_3 and r_4 are the thermal link from the source to the ground, including the thermal path through the quartz and teflon post, the thermal leakage through the electric connections and the heat transfer through radiation. For a fixed setup, these paths should be fixed. So by doing two sets of measurements, one set by only using V_1 as the source, the other by only using V_2 as source. We can get a set of equations:

$$\begin{aligned} V_1 &= i_1 \times (R_x + r_3) \\ V_1 &= j_1 \times r_4 \\ I_1 &= i_i + j_1 \\ V_2 &= i_2 \times r_3 \\ V_2 &= j_2 \times (R_x + r_4) \\ I_2 &= i_2 + j_2 \end{aligned}$$

where V_1 and V_2 are the temperature differences measured by the thermometers, I_1 and I_2 are the power input from the heater, which can be calculated from Joule heat. So among these six equations, we have seven unknowns: R_x, r_3, r_4, and i_1, i_2, the heat passed through r_3 path, and j_1, j_2, the heat passed through r_4 path.

To solve the problem, we need one more equations, which is obtained by turning on both heaters, but keep it in a way such that the temperature on the two quartz blocks are the same, i.e., there is no heat flowing through the crystal. In this way, we get two additional equations:

$$\begin{aligned} V_1' &= i_3 \times r_3 \\ V_2' &= j_3 \times r_4 \end{aligned}$$

In this way, we will get enough equations to solve all the unknowns, including the thermal conductance of the Mn_{12}-ac crystal.

We have constructed such a setup. But due to a technical problem with the cryostat which this setup was mounted on, we didn't get a chance to perform the actual measurement.

7.1.2 Relaxation rate at low temperature

The Mn_{12}-ac system exhibits hysteresis at low temperature as we mentioned before. This is due to a spin relaxation rate that is lower than the longitudinal field sweep rate, so that the system is driven out of equilibrium. Both thermal fluctuations and quantum fluctuations contribute to the spin relaxation process, but at high temperature the thermal fluctuations are the dominant effect. In the presence of transverse magnetic field and at very low temperature, there is a prediction that the system enters a regime where the quantum fluctuation becomes the dominant relaxation mechanism.

We performed a preliminary study trying to observe this behavior. We took a series of measurements with T ranging from 0.5 K to 4 K and $H_\perp$ ranging from 0.5 T to 3.5 T. Then we define the "open" area of the hysteresis loop as:

$$opening = \int_{H_{min}}^{H_{max}} (M_{sweeping\,up} - M_{sweeping\,down}) dH \tag{7.1}$$

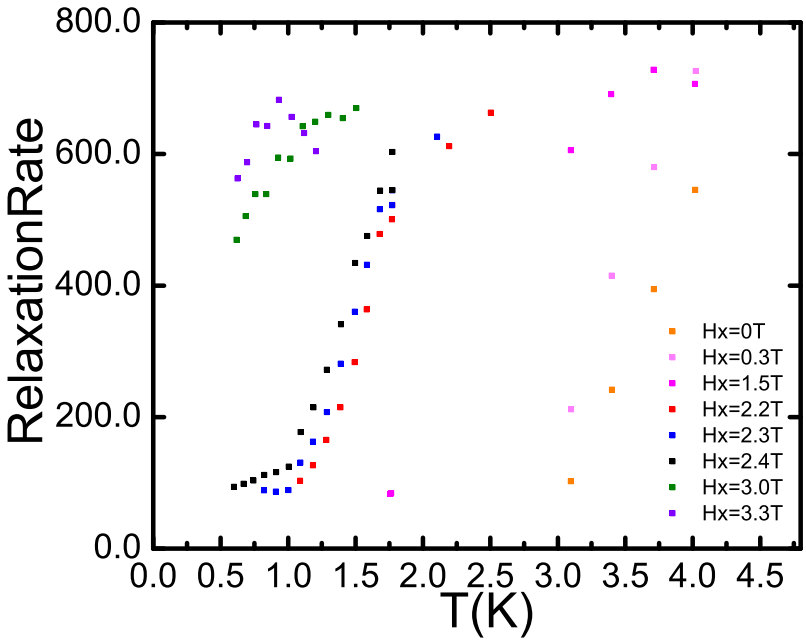

Figure 7.3: The opening area as a function of transverse magnetic field for selected temperatures.

where the $M_{sweeping\,up}$ is the magnetization recorded as the field increases, and $M_{sweeping\,down}$ is the magnetization recorded as the field decreases. Selected measurement data are shown in Fig. 7.3.

The relaxation of the magnetization of the sample can be modeled as:

$$dM/dt = \Gamma(T, H_t) \times (M - M_0) \tag{7.2}$$

where the Γ is the relaxation rate of the sample and it is a function of temperature and transverse field.

Γ is then related to our measurement data in the following way:

$$\begin{aligned} dM/dt &= dM/dH \times dH/dt \\ dM \times \frac{dH/dt}{\Gamma} &= (M - M_0) \times dH \\ \frac{dH/dt}{\Gamma} \int dM &= \int (M - M_0) dH = \frac{1}{2} opening \\ \therefore\ \Gamma &= \frac{2\, dH/dt \int dM}{opening} \end{aligned}$$

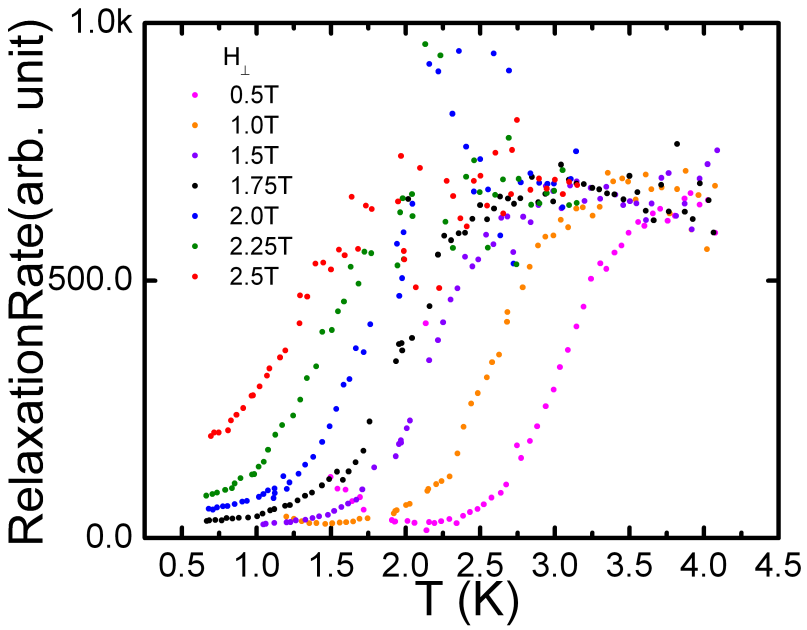

Figure 7.4: The relaxation rate as a function of temperature for selected magnetic fields.

where dH/dt is the sweep rate of the longitudinal field. The values of Γ calculated from the data are shown in Fig. 7.4.

As shown in Fig. 7.4, the relaxation rate is decreasing with the temperature because the thermal fluctuations become weaker. For 0.5 T, 1 T, 1.5 T, the rate saturates to a non-zero level, which indicates that the system may be entering the quantum fluctuation regime. However, the quality of the current data is insufficient to allow a definitive answer. For further study, we need access to lower temperatures so that we can observe the saturation for the higher transverse magnetic fields. In higher transverse field, the quantum fluctuations are stronger, so that the relaxation rate is expected to saturate at a higher value, which will give us a clearer signal to determine whether the system enters the quantum fluctuation regime.

7.1.3 Dipolar field calculation using molecular model

In Chapter 5, our calculation of the demagnetizing field is based on the assumption of uniform susceptibility. It is a general condition that can be applied in systems

other than Mn_{12}-ac, which makes this method capable of more general application. However, we also see that the result of the calculation did not fully catch all the details of the behavior of Mn_{12}-ac, especially the behavior at very low temperature.

Dmitry Garanin has provided a mathematical simulation model of the dipolar field of the Mn_{12}-ac system [83]. It considers the lattice structure and the magnetic properties of the Mn_{12}-ac single molecule giant spin. We can use this model instead of Eq. 5.5 to calculate the dipolar field distribution of the sample and then perform the same demagnetizing correction procedure to the data.

This may provide a better description of the system's low temperature behavior.

Chapter 8

Appendix

8.1 Appendix A. Magnetic field averaged over a rectangular surface

This section is a revised copy of the Appendix A of Pardo *et al.*: Demagnetizing factors for square bars (IEEE Transactions on magnetics, Vol. 40, No. 3, page 1491, May 2004), with the typos corrected and equations reformatted.

We derive the magnetic field generated by a rectangular plate with uniform surface pole density σ and averaged over a rectangular surface using the magnetic Coulomb law

$$H(r) = \frac{1}{4\pi\mu_0} \int_{S'} \frac{\sigma(r')(r-r')}{|r-r'|^3} dS' \tag{8.1}$$

We will only consider the field component perpendicular to the surface over which the average is made, according to the needs in (4) and (6). We call the magnetic field generated by the plate $H^{(\alpha)}$ with $\alpha = x$, y or z for the plate to be perpendicular to the x, y or z direction, respectively. The corresponding average over a rectangular surface is named as $\langle H^{(\alpha)} \rangle_\beta$ with $\beta = x$, y, or z for the surface to be perpendicular to the x, y or z direction, respectively.

$H^{(x)}$, $H^{(y)}$, and $H^{(z)}$ may be calculated by direct integration of the fields produced by point poles. Assuming the plate to be centered at the origin with dimensions $2a(y) \times 2b(z)$, $2a(z) \times 2b(x)$, and $2a(x) \times 2b(y)$ for the cases of $H^{(x)}$, $H^{(y)}$, and $H^{(z)}$

respectively, we obtain (Note that $F_2(z,x,y;a,b)\mathbf{j} = F_2(x,z,y;b,a)\mathbf{j}$. $H^{(y)}$ in original paper used second one.)

$$H^{(x)} = \frac{\sigma}{4\pi\mu_0}[F_1(y,z,x;a,b)\mathbf{j} + F_1(z,y,x;b,a)\mathbf{k} + F_2(y,z,x;a,b)\mathbf{i}] \tag{8.2}$$

$$H^{(y)} = \frac{\sigma}{4\pi\mu_0}[F_1(z,x,y;a,b)\mathbf{k} + F_1(x,z,y;b,a)\mathbf{i} + F_2(z,x,y;a,b)\mathbf{j}] \tag{8.3}$$

$$H^{(z)} = \frac{\sigma}{4\pi\mu_0}[F_1(x,y,z;a,b)\mathbf{i} + F_1(y,x,z;b,a)\mathbf{j} + F_2(x,y,z;a,b)\mathbf{k}] \tag{8.4}$$

where functions $F_1(u,v,w;t,d)$ and $F_2(u,v,w;t,d)$ are defined as (Note that In the paper, F_2 has a typo: $+f_2(u-t,v+d,w)$ should be $-f_2(u-t,v+d,w)$ or $f_2(t-u,v+d,w)$.)

$$F_1(u,v,w;t,d) = \tag{8.5}$$

$$+f_1(u+t,v-d,w) - f_1(u+t,v+d,w) + f_1(u-t,v+d,w) - f_1(u-t,v-d,w) \tag{8.6}$$

$$F_2(u,v,w;t,d) = \tag{8.7}$$

$$-f_2(u+t,v-d,w) + f_2(u+t,v+d,w) - f_2(u-t,v+d,w) + f_2(u-t,v-d,w) \tag{8.8}$$

functions $f_1(u',v',w')$ and $f_2(u',v',w')$ being

$$f_1(u',v',w') = \text{arcsinh}\frac{v'}{\sqrt{u'^2+w'^2}} \tag{8.9}$$

$$f_2(u',v',w') = \arctan\frac{u'v'}{w'\sqrt{u'^2+v'^2+w'^2}} \tag{8.10}$$

Once the field distribution is known, its average over a rectangular surface may be deduced by surface integration again. Assuming the rectangular surface to be centered at (x_0,y_0,z_0) with dimensions $2a'(y)\times 2b'(z)$, $2a'(z)\times 2b'(x)$, and $2a'(x)\times 2b'(y)$ for the cases of $\langle H^{(\alpha)}\rangle_x$, $\langle H^{(\alpha)}\rangle_y$, and $\langle H^{(\alpha)}\rangle_z$, respectively, we obtain (Note that $G_2(z_0,x_0,y_0;a,b,a',b') = G_2(x_0,z_0,y_0;b,a,b',a')$, in the paper $\langle H_y^{(y)}\rangle_y$ used the second

one.)

$$\langle H_x^{(x)}\rangle_x = \frac{\sigma}{16\mu_0\pi a'b'} G_2(y_0, z_0, x_0; a, b, a', b') \tag{8.11}$$

$$\langle H_y^{(x)}\rangle_y = \frac{\sigma}{16\mu_0\pi a'b'} G_1(y_0, z_0, x_0; a, b, a', b') \tag{8.12}$$

$$\langle H_z^{(x)}\rangle_z = \frac{\sigma}{16\mu_0\pi a'b'} G_1(z_0, y_0, x_0; b, a, b', a') \tag{8.13}$$

$$\langle H_x^{(y)}\rangle_x = \frac{\sigma}{16\mu_0\pi a'b'} G_1(x_0, z_0, y_0; b, a, b', a') \tag{8.14}$$

$$\langle H_y^{(y)}\rangle_y = \frac{\sigma}{16\mu_0\pi a'b'} G_2(z_0, x_0, y_0; a, b, a', b') \tag{8.15}$$

$$\langle H_z^{(y)}\rangle_z = \frac{\sigma}{16\mu_0\pi a'b'} G_1(z_0, x_0, y_0; a, b, a', b') \tag{8.16}$$

$$\langle H_x^{(z)}\rangle_x = \frac{\sigma}{16\mu_0\pi a'b'} G_1(x_0, y_0, z_0; a, b, a', b') \tag{8.17}$$

$$\langle H_y^{(z)}\rangle_y = \frac{\sigma}{16\mu_0\pi a'b'} G_1(y_0, x_0, z_0; b, a, b', a') \tag{8.18}$$

$$\langle H_z^{(z)}\rangle_z = \frac{\sigma}{16\mu_0\pi a'b'} G_2(x_0, y_0, z_0; a, b, a', b') \tag{8.19}$$

$$\tag{8.20}$$

where:

$$G_1(u, v, w; t_1, d_1, t_2, d_2) = g_1(u, v + t_2, w + d_2; t_1, d_1) - g_1(u, v - t_2, w + d_2, t_1, d_1) \tag{8.21}$$

$$- g_1(u, v + t_2, w - d_2, t_1, d_1) + g_1(u, v - t_2, w - d_2, t_1, d_1) \tag{8.22}$$

$$G_2(u, v, w; t_1, d_1, t_2, d_2) = g_2(u + t_2, v + d_2, w; t_1, d_1) - g_2(u + t_2, v - d_2, w; t_1, d_1) \tag{8.23}$$

$$- g_2(u - t_2, v + d_2, w; t_1, d_1) + g_2(u - t_2, v - d_2, w; t_1, d_1) \tag{8.24}$$

functions $g_1(u', v', w'; t', d')$ and $g_2(u', v', w'; t', d')$ being defined as

$$g_1(u', v', w'; t', d') = + \tilde{f}_1(u' + t', v' - d', w') - \tilde{f}_1(u' + t', v' + d', w') \tag{8.25}$$

$$+ \tilde{f}_1(u' - t', v' + d', w') - \tilde{f}_1(u' - t', v' - d', w') \tag{8.26}$$

$$g_2(u', v', w'; t', d') = - \tilde{f}_2(u' + t', v' - d', w') + \tilde{f}_2(u' + t', v' + d', w') \tag{8.27}$$

$$- \tilde{f}_2(u' - t', v' + d', w') + \tilde{f}_2(u' - t', v' - d', w') \tag{8.28}$$

with

$$\tilde{f}_1(u'',v'',w'') = -u''v''\arctan\frac{v''w''}{u''\sqrt{u''^2+v''^2+w''^2}} - \frac{w''}{2}\sqrt{u''^2+v''^2+w''^2} \quad (8.29)$$

$$+ v''w''\text{arcsinh}\frac{v''}{\sqrt{u''^2+w''^2}} + \frac{v''^2-u''^2}{2}\text{arcsinh}\frac{w''}{\sqrt{u''^2+v''^2}} \quad (8.30)$$

$$\tilde{f}_2(u'',v'',w'') = u''v''\arctan\frac{u''v''}{w''\sqrt{u''^2+v''^2+w''^2}} - w''\sqrt{u''^2+v''^2+w''^2} \quad (8.31)$$

$$+ u''w''\text{arcsinh}\frac{u''}{\sqrt{v''^2+w''^2}} + v''w''\text{arcsinh}\frac{v''}{\sqrt{u''^2+w''^2}} \quad (8.32)$$

8.2 Appendix B. Anisotropy in Mn_{12}

Mn_{12} system has a strong easy-axis is an anisotropy system. The c-axis is the easy direction, i.e., $\chi_{zz} > \chi_{xx} = \chi_{yy}$. The single ion anisotropy, $A = \chi_{zz}/\chi_{xx} = \frac{\Delta\langle S_z\rangle}{\Delta H_z}/\frac{\Delta\langle S_x\rangle}{\Delta H_x}$, can be estimated by the single ion Hamiltonian:

$$\hat{\mathcal{H}} = -DS_z^2 - BS_z^4 - g\mu_B H_z S_z + g\mu_B H_T S_x \quad (8.33)$$

where $D = 0.548$ K, $B = 0.0012$ K. Fig. 8.1 shows the A verses temperature for different H_t. In the following procedures, we assume that the single ion anisotropy is a good approximation of the crystal anisotropy.

In the paper of Shiqi et al. [62], we measured the crystal longitudinal susceptibility $\chi_{zz} = \partial M_z/\partial H_z|_{H_z=0}$ using MPMS for a group of crystals with different aspect ratio. After plotting the T_{cw} as a function of sample aspect ratio, we can extrapolate the data to obtain an infinite length sample's T_{cw}, which by definition is demag corrected. The other conclusion of Shiqi et al. is that the slope of inverse susceptibility verses temperature between 3K and 6K is independent of sample aspect ratio. Using the demag-corrected T_{cw} and slope, we are able to normalize the parameter of Millis et al.'s mean field theory model [21], to obtain the susceptibility's temperature dependent for $H_t = 0$T for all the temperature, as shown in Fig. 8.2 for Mn_{12}-ac case. A linear fit to the solid lines between 3K and 6K will give a slope of ~ 0.57 and a temperature intercept about ~ 0.85 K, reassembling the MPMS data's prediction for

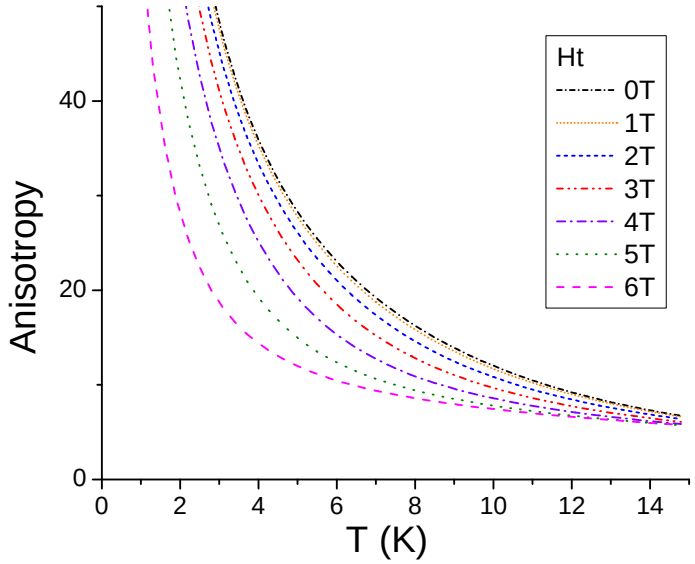

Figure 8.1: Mn_{12}-ac single ion anisotropy vs temperature under different transverse fields

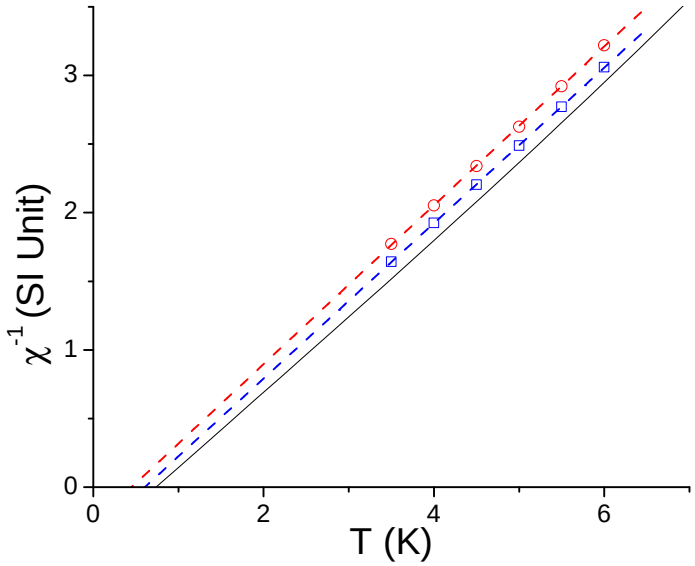

Figure 8.2

infinite aspect ratio sample. (For Mn_{12}-ac-MeOH case, we can obtain similar result with slope ~ 0.59 and intercept ~ 0.74 K.)

With both anisotropy and χ_{zz} at hand, we have the full information of susceptibility for zero transverse field. In the next step, we utilize the finite element method to calculate the expected Hall sensor reading at the corresponding sensor locations and

compare them with the experimental readings.

We consider a rectangle prismwith a constant intrinsic (local) susceptibility:

$$\chi = \begin{pmatrix} \chi_{xx} & 0 & 0 \\ 0 & \chi_{yy} & 0 \\ 0 & 0 & \chi_{zz} \end{pmatrix}, \tag{8.34}$$

where $\chi_{ij} = \partial M_i/\partial H_j|_{H_j=0}$. Since the material has a constant susceptibility, the local magnetization M(r) and magnetic field H(r) are determined by the surface pole distribution $\sigma(r)$ [84, 85].

To calculate $\sigma(r)$ we first divide the surface into n elements, each having a uniform surface pole density σ^i. Using $\sigma/\mu_0 = \mathbf{M} \cdot \hat{k} = \chi(\mathbf{H}_a + \mathbf{H}_d) \cdot \hat{k}$, $\hat{k}$ being the outward unit vector normal to the surface, and taking into account that σ is the only source of the local demagnetizing field $\mathbf{H}_d$ we find that

$$\frac{\sigma^i}{\chi_{kk}\mu_0} + \sum_{j=1}^{n} \hat{k}^i \cdot \mathbf{D}^{ij} \frac{\sigma^j}{\mu_0} = \hat{k}^i \cdot \mathbf{H}_a, \tag{8.35}$$

where $\hat{k}^i$ is the outward unit vector normal to the ith element (equals to $\hat{x}$, $\hat{y}$, or $\hat{z}$), the χ_{kk} is the susceptibility corresponding to the $\hat{k}^i$ direction and $\mathbf{D}^{ij}\frac{\sigma^j}{\mu_0}$ is the negative of the demagnetizing field generated by the jth element, as derived in Appendix A.

Bibliography

[1] J. M. Luttinger and L. Tisza, *Phys. Rev.*, **70**(11-12), 954–964 (1946).

[2] M. R. Roser and L. R. Corruccini, *Phys. Rev. Lett.*, **65**(8), 1064–1067 (1990).

[3] Eugene M. Chudnovsky and Javier Tejada, *Lectures on Magnetism with 128 Problems*, Rinton Press, 2006.

[4] Jonathan R. Friedman, M. P. Sarachik, J. Tejada, and R. Ziolo, *Phys. Rev. Lett.*, **76**(20), 3830–3833 (1996).

[5] L. Thomas, F. Lionti, R. Ballou, D. Gatteschi, R. Sessoli, and B. Barbara, *Nature (London)*, **383**, 145–147 (1996).

[6] J. M. Hernandez, X. X. Zhang, F. Luis, J. Tejada, Jonathan R. Friedman, M. P. Sarachik, and R. Ziolo, *Phys. Rev. B*, **55**(9), 5858–5865 (1997).

[7] C. Sangregorio, T. Ohm, C. Paulsen, R. Sessoli, and D. Gatteschi, *Phys. Rev. Lett.*, **78**, 4645–4648 (1997).

[8] Sheila M. J. Aubin, Neil R. Dilley, Luca Pardi, J. Krzystek, Michael W. Wemple, Louis-Claude Brunel, M. Brian Maple, George Christou, and David N. Hendrickson, *Journal of the American Chemical Society*, **120**(20), 4991–5004 (1998).

[9] Hanspeter Andres, Reto Basler, Alexander J. Blake, Cyril Cadiou, Gregory Chaboussant, Craig M. Grant, Hans-Ulrich Güdel, Mark Murrie, Simon Parsons, Carley Paulsen, Fabrizzio Semadini, Vincent Villar, Wolfgang Wernsdorfer, and Richard E. P. Winpenny, *Chem. Eur. J.*, **8**(21), 4867–4876 (2002).

[10] Euan K. Brechin, Colette Boskovic, Wolfgang Wernsdorfer, Jae Yoo, Akira Yamaguchi, E. Carolina Saüdo, Thomas R. Concolino, Arnold L. Rheingold, Hidehiko Ishimoto, David N. Hendrickson, and George Christou, *J. Am. Chem. Soc.*, **124**(33), 9710–9711 (2002).

[11] I. Chiorescu, W. Wernsdorfer, A. Müller, H. Bögge, and B. Barbara, *Phys. Rev. Lett.*, **84**, 3454–3457 (2000).

[12] W. Wernsdorfer and R. Sessoli, *Science*, **284**(5411), 133–135 (1999).

[13] W Wernsdorfer, I Chiorescu, R Sessoli, D Gatteschi, and D Mailly, *Physica B: Condensed Matter*, **284 - 288, Part 2**(0), 1231 – 1232 (2000).

[14] A. Morello, F. L. Mettes, F. Luis, J. F. Fernández, J. Krzystek, G. Aromí, G. Christou, and L. J. de Jongh, *Phys. Rev. Lett.*, **90**(1), 017206 (2003).

[15] M. Evangelisti, F. Luis, F. L. Mettes, N. Aliaga, G. Aromí, J. J. Alonso, G. Christou, and L. J. de Jongh, *Phys. Rev. Lett.*, **93**(11), 117202 (2004).

[16] F. Luis, J. Campo, J. Gómez, G. J. McIntyre, J. Luzón, and D. Ruiz-Molina, *Phys. Rev. Lett.*, **95**(22), 227202 (2005).

[17] M. Evangelisti et al., *Phys. Rev. Lett.*, **97**(16), 167202 (2006).

[18] Julio F. Fernández and Juan José Alonso, *Phys. Rev. B*, **62**(1), 53–56 (2000).

[19] D. A. Garanin and E. M. Chudnovsky, *Phys. Rev. B*, **78**(17), 174425 (2008).

[20] Bo Wen, P. Subedi, Lin Bo, Y. Yeshurun, M. P. Sarachik, A. D. Kent, A. J. Millis, C. Lampropoulos, and G. Christou, *Phys. Rev. B*, **82**(1), 014406 (2010).

[21] A. J. Millis, A. D. Kent, M. P. Sarachik, and Y. Yeshurun, *Phys. Rev. B*, **81**, 024423 (2010).

[22] S. Fishman and A. Aharony, *J. Phys. C: Solid State Phys.*, **12**(18), L729–L733 (1979).

[23] D. M. Silevitch, D. Bitko, J. Brooke, S. Ghosh, G. Aeppli, and T. F. Rosenbaum, *Nature*, **448**(7153), 567–570 (2007).

[24] Moshe Schechter, *Phys. Rev. B*, **77**(2), 020401 (2008).

[25] R. Giraud, A. M. Tkachuk, and B. Barbara, *Phys. Rev. Lett.*, **91**(25), 257204 (2003).

[26] M. Schechter and P. C. E. Stamp, *Phys. Rev. Lett.*, **95**(26), 267208 (2005).

[27] E. del Barco, A. D. Kent, E. M. Rumberger, D. N. Hendrickson, and G. Christou, *Phys. Rev. Lett.*, **91**(4), 047203 (2003).

[28] S. Hill, R. S. Edwards, S. I. Jones, N. S. Dalal, and J. M. North, *Phys. Rev. Lett.*, **90**(21), 217204 (2003).

[29] S. Takahashi, R. S. Edwards, J. M. North, S. Hill, and N. S. Dalal, *Phys. Rev. B*, **70**(9), 094429 (2004).

[30] E. del Barco, A. D. Kent, S. Hill, J. M. North, N. S. Dalal, E. M. Rumberger, D. N. Hendrickson, N. Chakov, and G. Christou, *J. Low Temp. Phys.*, **140**(1-2), 119–174 (2005).

[31] Kyungwha Park, Tunna Baruah, Noam Bernstein, and Mark R. Pederson, *Phys. Rev. B*, **69**(14), 144426 (2004).

[32] T. Lis, *Acta Cryst. B*, **36**(9), 2042–2046 (1980).

[33] Andrea Cornia, Antonio Costantino Fabretti, Roberta Sessoli, Lorenzo Sorace, Dante Gatteschi, Anne-Laure Barra, Carole Daiguebonne, and Thierry Roisnel, *Acta Cryst. Sec. C*, **58**(7), m371–m373 (2002).

[34] G. Redler, C. Lampropoulos, S. Datta, C. Koo, T. C. Stamatatos, N. E. Chakov, G. Christou, and S. Hill, *Phys. Rev. B*, **80**(9), 094408 (2009).

[35] T. C. Stamatatos, K. A. Abboud, and G. Christou. unpublished.

[36] Andrea Caneschi, Dante Gatteschi, Roberta Sessoli, Anne Laure Barra, Louis Claude Brunel, and Maurice Guillot, *Journal of the American Chemical Society*, **113**(15), 5873–5874 (1991).

[37] Roberta Sessoli, Hui Lien Tsai, Ann R. Schake, Sheyi Wang, John B. Vincent, Kirsten Folting, Dante Gatteschi, George Christou, and David N. Hendrickson, *Journal of the American Chemical Society*, **115**(5), 1804–1816 (1993).

[38] Roberta Sessoli, *Molecular Crystals and Liquid Crystals Science and Technology. Section A. Molecular Crystals and Liquid Crystals*, **274**(1), 145–157 (1995).

[39] Anne Laure Barra, Andrea Caneschi, Dante Gatteschi, and Roberta Sessoli, *Journal of the American Chemical Society*, **117**(34), 8855–8856 (1995).

[40] Anne Laure Barra, Dante Gatteschi, and Roberta Sessoli, *Phys. Rev. B*, **56**, 8192–8198 (1997).

[41] S. Hill, J. A. A. J. Perenboom, N. S. Dalal, T. Hathaway, T. Stalcup, and J. S. Brooks, *Phys. Rev. Lett.*, **80**, 2453–2456 (1998).

[42] A. Caneschi, T. Ohm, C. Paulsen, D. Royal, C. Sangregorio, and R. Sessolia, *J. Magn. Magn. Mater.*, **177-181**(Part 2), 1330 – 1336 (1998).

[43] M. R. Pederson and S. N. Khanna, *Phys. Rev. B*, **59**, R693–R696 (1999).

[44] M. R. Pederson and S. N. Khanna, *Phys. Rev. B*, **60**, 9566–9572 (1999).

[45] Jose Ramón Galán-Mascarós, Carlos J. Gómez-Garcia, Juan José Borrás-Almenar, and Eugenio Coronado, *Advanced Materials*, **6**(3), 221–223 (1994).

[46] R. S. Edwards, S. Maccagnano, E.-C. Yang, S. Hill, W. Wernsdorfer, D. Hendrickson, and G. Christou, *J. Appl. Phys.*, **93**(10), 7807–7809 (2003).

[47] A. Wilson, J. Lawrence, E-C. Yang, M. Nakano, D. N. Hendrickson, and S. Hill, *Phys. Rev. B*, **74**, 140403 (2006).

[48] Achim Müller, Erich Krickemeyer, Jochen Meyer, Hartmut Bögge, Frank Peters, Winfried Plass, Ekkehard Diemann, Stephan Dillinger, Fritz Nonnenbruch, Markus Randerath, and Carst Menke, *Angew. Chem. Int. Ed. in English*, **34**(19), 2122–2124 (1995).

[49] Achim Müller, Erich Krickemeyer, Hartmut Bögge, Marc Schmidtmann, Christian Beugholt, Paul Kögerler, and Canzhong Lu, *Angew. Chem. Int. Ed.*, **37**(9), 1220–1223 (1998).

[50] M. A. Novak, R. Sessoli, A. Caneschi, and D. Gatteschi, *J. Magn. Magn. Mater.*, **146**(1-2), 211–213 (1995).

[51] A. M. Gomes, M. A. Novak, R. Sessoli, A. Caneschi, and D. Gatteschi, *Phys. Rev. B*, **57**, 5021–5024 (1998).

[52] R. Blinc, B. Zalar, A. Gregorovič, D. Arčon, Z. Kutnjak, C. Filipič, A. Levstik, R. M. Achey, and N. S. Dalal, *Phys. Rev. B*, **67**, 094401 (2003).

[53] Jonathan Friedman. *Resonant Magnetization Tunneling in High-Spin Molecules.* PhD thesis, The City University of New York, 1996.

[54] W. Wernsdorfer, R. Sessoli, and D. Gatteschi, *Europhys. Lett.*, **47**(2), 254–259 (1999).

[55] F. Luis, J. Bartolomé, J. F. Fernández, J. Tejada, J. M. Hernández, X. X. Zhang, and R. Ziolo, *Phys. Rev. B*, **55**, 11448–11456 (1997).

[56] J. A. A. J. Perenboom, J. S. Brooks, S. Hill, T. Hathaway, and N. S. Dalal, *Phys. Rev. B*, **58**, 330–338 (1998).

[57] D. A. Garanin and E. M. Chudnovsky, *Phys. Rev. B*, **56**(17), 11102–11118 (1997).

[58] D A Garanin, *Journal of Physics A: Mathematical and General*, **24**(2), L61 (1991).

[59] A. Cornia, R. Sessoli, L. Sorace, D. Gatteschi, A. L. Barra, and C. Daiguebonne, *Phys. Rev. Lett.*, **89**, 257201 (2002).

[60] W.F. Brown, *Magnetostatic principles in ferromagnetism*, Selected topics in solid state physics, North-Holland Pub. Co., 1962.

[61] Soshin Chikazumi, *Physics of Ferromagnetism*, Oxford University Press, 2005.

[62] Shiqi Li, Lin Bo, Bo Wen, M. P. Sarachik, P. Subedi, A. D. Kent, Y. Yeshurun, A. J. Millis, C. Lampropoulos, S. Mukherjee, and G. Christou, *Phys. Rev. B*, **82**(17), 174405 (2010).

[63] E. Pardo, Du-Xing Chen, and A. Sanchez, *Magnetics, IEEE Transactions on*, **40**(3), 1491 – 1498 (2004).

[64] D.-X. Chen, E. Pardo, and A. Sanchez, *Magnetics, IEEE Transactions on*, **41**(6), 2077 – 2088 (2005).

[65] Rashmi Bagai and George Christou, *Chem. Soc. Rev.*, **38**, 1011 – 1026 (2009).

[66] B. Wen, P. Subedi, L. Bo, Y. Yeshurun, M. P. Sarachik, A. D. Kent, A. J. Millis, C. Lampropoulos, and G. Christou. Realization of random-field Ising ferromagnetism in a molecular magnet. arXiv:0910.1754, Oct 2009.

[67] P. Subedi, A. D. Kent, Bo Wen, M. P. Sarachik, Y. Yeshurun, A. J. Millis, S. Mukherjee, and G. Christou, *Phys. Rev. B*, **85**, 134441 (2012).

[68] E. D. Hall, *Am. J. Math*, **2**, 287 (1879).

[69] Jonathan R. Friedman, *Phys. Rev. B*, **57**(17), 10291–10294 (1998).

[70] Yoseph Imry and Shang-keng Ma, *Phys. Rev. Lett.*, **35**(21), 1399–1401 (1975).

[71] Yoseph Imry and Michael Wortis, *Phys. Rev. B*, **19**(7), 3580–3585 (1979).

[72] D.P. Belanger and A.P. Young, *J. Magn. Magn. Mater.*, **100**(1-3), 272 – 291 (1991).

[73] Kyungwha Park, M. A. Novotny, N. S. Dalal, S. Hill, and P. A. Rikvold, *Phys. Rev. B*, **66**(14), 144409 (2002).

[74] S. McHugh, R. Jaafar, M. P. Sarachik, Y. Myasoedov, H. Shtrikman, E. Zeldov, R. Bagai, and G. Christou, *Phys. Rev. B*, **79**(5), 052404 (2009).

[75] John D. Jackson. *Classical Electrodynamics Third Edition - Eq. (5.100)*, chapter 5, page 197. Wiley, 1998.

[76] Jonathan R. Friedman, M. P. Sarachik, J. M. Hernandez, X. X. Zhang, J. Tejada, E. Molins, and R. Ziolo, *J. Appl. Phys.*, **81**(8), 3978 –3980 (1997).

[77] E. Burzurí, F. Luis, B. Barbara, R. Ballou, E. Ressouche, O. Montero, J. Campo, and S. Maegawa, *Phys. Rev. Lett.*, **107**, 097203 (2011).

[78] Sean McHugh. *Magnetic deflagration in the molecular magnet Mn12-ac*. PhD thesis, CUNY-CCNY, GC, 2009.

[79] A. C. Anderson, W. Reese, and J. C. Wheatley, *Review of Scientific Instruments*, **34**(12), 1386–1390 (1963).

[80] R. C. Zeller and R. O. Pohl, *Phys. Rev. B*, **4**, 2029–2041 (1971).

[81] Barucci M., Gottardi E., Olivieri E., Pasca E., Risegari L., and Ventura G., *Cryogenics*, **42**(9), 551–555 (2002).

[82] J.P. Le E.D. Marquardt and Ray Radebaugh. Cryogenic material properties database. 11th International Cryocooler Conference, June 2000.

[83] D. A. Garanin. Theory of deflagration and fronts of tunneling in molecular magnets. Eq.(1.54) of arXiv:1211.4192.

[84] D.-X. Chen, J.A. Brug, and R.B. Goldfarb, *Magnetics, IEEE Transactions on*, **27**(4), 3601 –3619 (1991).

[85] Enric Pardo, Alvaro Sanchez, and Du-Xing Chen, *J. Appl. Phys.*, **91**(8), 5260 –5267 (2002).